Experiments on vertical plane buoyant jets in shallow water

By JANNIS ANDREOPOULOS,† ANANDA PRATURI‡
AND WOLFGANG RODI

Institut für Hydromechanik, University of Karlsruhe, Karlsruhe, F.R. Germany

The paper reports on measurements of the flow generated by a plane buoyant jet discharging vertically into shallow water. The study comprises visualization experiments, mean-velocity and turbulence measurements with a two-channel laser-Doppler anemometer and temperature measurements with thermistor probes. According to the previous investigation of Jirka & Harleman (1979) (JH) the flow may be either stable with the heated discharge water leaving the near field in a warm water layer adjacent to the surface, or unstable with flow recirculation and re-entrainment of heated water into the jet. The stable situation usually involves an internal hydraulic jump associated with a roller. Both stable and unstable situations were investigated, the limiting case of a non-buoyant jet representing the unstable one. In order that a roller representing an internal hydraulic jump developed in the relatively short test channel in the buoyant situations, a strong downstream control had to be imposed by inserting a slightly submerged weir. Most experiments were carried out at a depth-to-discharge-width ratio of 100, and in this case the strong upstream control caused the hydraulic jump to be flooded for both of the densimetric Froude numbers studied ($F = 9.9$ and 21). In each case, a thick upper layer of nearly uniform temperature developed, with a larger layer thickness for $F = 21$. Below this layer was a relatively thin interface with temperature gradients and below this a counterflow of cold ambient water. For both Froude numbers, the flow was stable in the sense of JH, but only marginally so in the higher-Froude-number case. The observed trends of the flow behaviour follow the stability analysis of JH, but the dilution of the heated water, which was determined from the temperature measurements, is different from that predicted by the JH mixing analysis. The dilution is much lower in the present case with the flooded jump than in the JH analysis and experiments without specific downstream control and with a much longer test channel and thus no flooded jump.

1. Introduction

Many industrial processes generate waste water which is often discharged into natural water bodies, be it rivers, lakes or coastal waters. There is therefore considerable interest in the design, performance and control of such discharges as well as in their impact on the environment. A case of particular significance is the discharge into a shallow-water body from a line source (e.g. a multiport diffusor)

† Present address: Department of Mechanical Engineering, The City College of the City University of New York, NY 10031, USA.
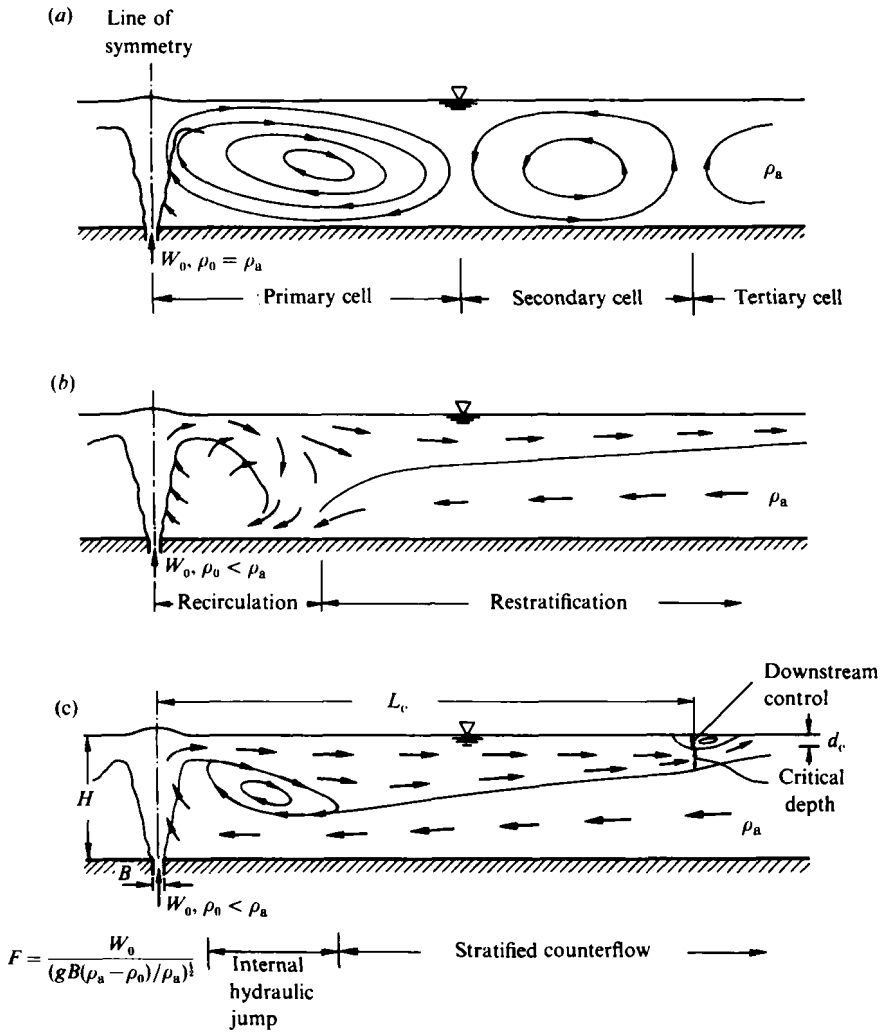‡ Present address: Tektronix, Beaverton, Oregon, USA.

(a) Line of
      symmetry

$W_0, \rho_0 = \rho_a$

—— Primary cell ——+—— Secondary cell —+—— Tertiary cell

(b)

$W_0, \rho_0 < \rho_a$

—— Recirculation ——+—————— Restratification ————→

(c)

$$F = \frac{W_0}{(gB(\rho_a - \rho_0)/\rho_a)^{\frac{1}{2}}}$$

—— Internal
    hydraulic
    jump

—— Stratified counterflow ——→

FIGURE 1. Examples of steady-state flows for vertical-jet discharges into shallow water:
(a) non-buoyant (unstable); (b) weakly buoyant (unstable); (c) strongly buoyant (stable).

placed at the bottom, where the confinement of the flow domain has a significant influence on the flow development. An extensive review of such discharge situations and their use for heat disposal has been given by Jirka (1982a) who covers a wide range of different situations. The present study is concerned with the special case of a two-dimensional, vertical discharge from a line source without considering end effects and without crossflow. A symmetrical flow develops, with the plane vertical discharge jet being deflected at the surface and a wide range of flow patterns developing in the shallow-water body. These patterns depend mainly on the buoyancy of the discharge characterized by the densimetric Froude number F (defined in figure 1), the ratio of water depth to discharge width H/B and the downstream control of the flow. The main examples are sketched in figure 1.

A theoretical analysis of this flow situation and the influence of various parameters was provided by Jirka & Harleman (1979) and was later summarized by Jirka (1982b). According to the authors' knowledge, the first paper also reports on the only

experimental study carried out on this flow situation. This study was restricted to visualization experiments and temperature measurements and does not provide any information on the velocity field; it also did not investigate the influence of an imposed downstream control. The present work studies the effect of a downstream-control weir and provides further experimental results, including details of the velocity distribution and the turbulence field, in order to make available data obtained under well-controlled conditions for validating calculation methods for this complex flow involving a number of interesting physical phenomena.

The paper reports on measurements for non-buoyant situations ($F = \infty$) at two Reynolds numbers and on a second set of experiments at two different densimetric Froude numbers (the Reynolds number also being different in each case). Most of the experiments were carried out at $H/B = 100$. The experimental programme consisted of flow-visualization studies, velocity measurements with a two-channel laser-Doppler anemometer (LDA) and temperature measurements with thermistor probes. Section 2 discusses the general characteristics of the flow considered. The experimental set-up and measurement techniques are described in §3. The flow-visualization studies are presented and discussed in §4 and the detailed measurements in §5. The paper ends with conclusions in §6.

2. General flow characteristics

A brief review is given here of the available information on vertical buoyant jets in shallow waters. This review is based mainly on the analysis and the measurements of Jirka & Harleman (1979, hereinafter referred to as JH). These authors distinguish between various flow regimes, which differ according to the parameter situation considered and which will now be discussed in some details. In all cases, whether buoyant or non-buoyant, a vertical jet develops which spreads and entrains ambient fluid. The rate of entrainment depends on the buoyancy of the jet but also on the development of the ambient flow. The jet impinges on the free surface, thereby causing a small superelevation which in turn leads to an excess hydrostatic pressure that drives the fluid sideways away from the impingement region. This impingement process is very similar to that on a solid wall, the difference being that in the latter case there is of course no deformation of the surface but a rise in static pressure which drives the flow sideways.

After the surface deflection of the jet, the flow development depends strongly on the parameter situation considered. First we discuss the case of a non-buoyant discharge sketched in figure 1 (a). Owing to the shallowness of the ambient water, not all of the fluid that the jet wants to entrain can be supplied by the undisturbed ambient; rather the entrainment flow sets up a pressure distribution such that the horizontal surface jet is turned downward and a large part of its fluid is re-entrained, forming a recirculation zone as shown in figure 1 (a). This zone forms a secondary counter-rotating zone by momentum transfer at its outer boundary and this forms a third one and so on. The size of the cells and the strength of their rotation decreases for the higher-order cells. According to JH, the primary zone has a length of 2–2.5H. The second cell is already considerably shorter and weaker; it has in fact not been observed in the flow-visualization experiments of JH.

For buoyant jet discharges, JH distinguish between stable and unstable situations. When the jet is weakly buoyant and the ratio H/B is small, the jet entrainment again causes a recirculation in the near field as sketched in figure 1 (b) and hence re-entrainment of the heated near-surface fluid. This situation with recirculation

occurring in the discharge vicinity is classified by JH as unstable. Of course, the non-buoyant situation is also unstable. The re-entrainment of heated fluid grossly reduces the dilution abilities of the discharge system and hence is less ideal from an environmental point of view. In contrast to the non-buoyant situation sketched in figure 1(*a*), no secondary cell is formed; rather, a stratified two-layer counterflow develops in which heated fluid leaves the area of interest and, underneath, cold ambient fluid flows towards the discharge and mixes with the fluid turning down from the surface layer before it is entrained into the jet. The stratified counterflow is controlled by downstream events, as will be discussed below.

For strongly buoyant discharges and when the ratio H/B is relatively large, after the deflection the heated fluid does not turn downward to be re-entrained, but a stratified two-layer counterflow develops which does not communicate with the vertical buoyant-jet zone. In this case, the flow in the lower layer provides all the fluid entrained into the jet. This is classified as a stable situation by JH. Since no re-entrainment occurs, the dilution of such a system is much higher. Several different evolutions of the two-layer system are possible, as was analysed in detail by Wilkinson & Wood (1971). The following description is based mainly on their analysis and supporting measurements as well as on the experimental study of Baddour & Chu (1975). In cases with no or negligible downstream control on the two-layer flow, the upper, outward-flowing layer, which forms a surface jet, entrains fluid from the lower layer. The surface-jet flow is supercritical, i.e. the densimetric Froude number based on the local layer thickness, velocity, and density difference to the ambient is larger than 1. The Froude number decreases continuously in the downstream direction and the entrainment is reduced due to the growing influence of the stable stratification. When the Froude number has fallen to a value of 1, a critical state is reached where entrainment stops and the upper layer has a critical depth and maximum discharge. Usually some downstream control is imposed, for example by interfacial friction or a downstream structure like the end of the tank (as in the experiments of JH) or a weir. All of these controls have a blockage effect which reduces the critical depth and hence the maximum possible discharge of the upper layer. Since this maximum discharge is equal to the jet discharge plus the total entrainment into the vertical and surface jet, the entrainment must be reduced when the maximum discharge is lower. This reduction is brought about by an internal hydraulic jump which is established somewhere between the impingement region and the critical control region (see figure 1c). Experiments (Wilkinson & Wood 1971; Baddour & Chu 1975; Rajaratnam & Subramanyan 1985) have shown that significant entrainment into the surface layer takes place only until the jump occurs; the jump itself is associated with a roller which causes intense mixing in the upper layer but shields this from the lower layer so that there is very little entrainment in the jump region. In the jump, the supercritical upstream flow undergoes fairly rapid transition to a sub-critical flow with local Froude numbers smaller than 1, and a stratified counterflow develops downstream of the jump in which there is also no entrainment. The jump occurs at the position where the entrainment into the vertical buoyant jet and into the bent-over horizontal surface jet, together with the jet discharge, has reached the maximum discharge determined by the downstream control. The length of the internal hydraulic jump was first estimated by Mehrota (1976) to be of the order of $2H$.

When the downstream control becomes stronger, i.e. when the blockage effect is increased, the maximum discharge is reduced and the jump moves towards the vertical jet until it occurs immediately after the bending-over of the jet. If the

blockage effect is increased even more, entrainment can only be reduced further by also inhibiting entrainment into the vertical jet, which happens by the occurrence of a submerged (or flooded) jump that interacts directly with the upper part of the vertical jet and inhibits the entrainment of ambient fluid in this region. In this case the upper layer in which heated water is present is quite thick from the beginning. The roller now interacts with the jet and causes the temperature to be fairly uniform over the upper part of the jet and also in the upper surface layer. Of course, the dilution is much smaller in this case than when the jump is not flooded. If the jump depth increases further, e.g. by having even more blockage, the two-layer structure in the jet vicinity is destroyed and fluid from the upper, warmer layer is entrained into the jet near the bottom. This is then the unstable case described above (and sketched in figure 1b). Hence the flooded jump is a transition from the stable to the unstable discharge situation, as indicated by JH. In their experiments, JH did not impose a specific downstream control and did not observe any flooded jumps. However, in an analogous later study on round buoyant jets in shallow water, Lee & Jirka (1981) did observe the occurrence of submerged (radial) jumps and found the associated flows to be on the borderline between stability and instability.

It is of interest to note here that, in their experiments on buoyant underflows (discharge of a wall jet) in shallow water, Baddour & Abbink (1983) observed the same type of flow situations as did JH and Lee & Jirka (1981) in their vertical-buoyant-jet-in-shallow-water studies. For weakly buoyant discharges and lower ratios of water depth to jet width an unstable flow developed, while for strongly buoyant jets and larger depth to jet-width ratios a stable situation developed in general. This could involve either a free internal hydraulic jump or a flooded jump depending on the downstream control, which was imposed by a lateral contraction at the end of the test channel. By increasing this contraction, keeping all other parameters constant, the free jump moved upstream, then got flooded, and finally a transition from a flooded jump to an unstable flow situation with re-entrainment occurred. In the vertical jet-in-shallow-water experiments reported here, flooded jumps were produced by placing a submerged weir of depth d_c in the test channel (see figure 1c).

3. Experimental techniques

3.1. *Experimental set-up*

The experimental arrangement of the present study is shown schematically in figure 2. The buoyant-jet-in-shallow-water experiment required a test channel which is connected to a relatively large reservoir providing ambient water under virtually constant conditions. This arrangement was achieved by placing a dividing wall of 4.4 m × 1.2 m into a tank of 6 m length, 2.1 m width and 1.2 m height. The test channel, of width 30 cm, is formed by the dividing wall and the front wall of the reservoir, which contains three glass windows. The water depth in the channel is controlled by an overflow weir at the back of the reservoir. The height of this weir and hence the water level can be adjusted in increments of 15 cm from a minimum water depth of 15.5 cm to a maximum depth of 105.5 cm. Cold make-up water was supplied through a manifold of 10 spray nozzles (marked × in figure 2) in order to keep the water temperature in the reservoir constant despite the heated water flowing from the test-channel section into the reservoir. Two thermistors (T_{11} and T_{12}) are positioned in the front-lower corners of the reservoir to record the ambient water temperature. The reservoir is filled with cold water from the main water supply by
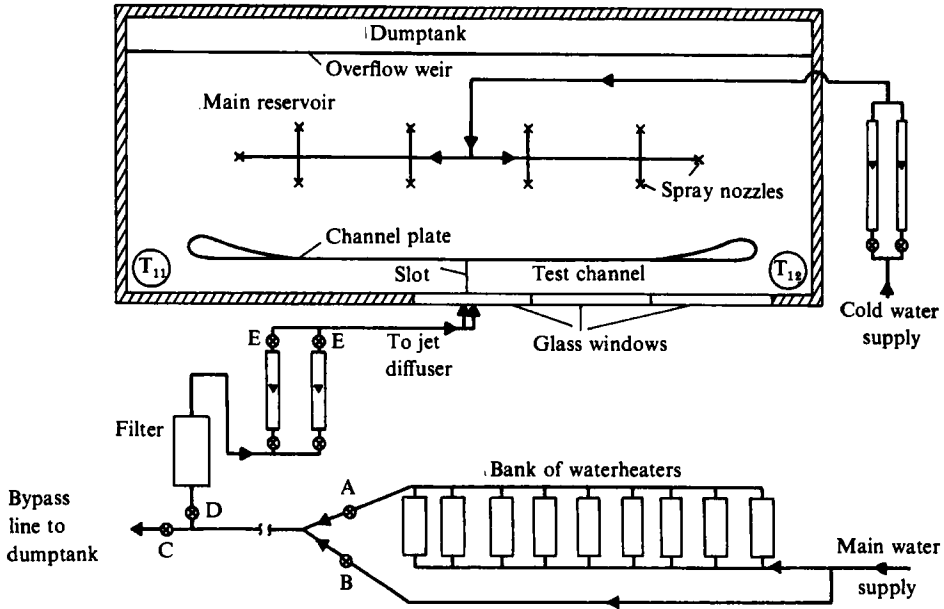
FIGURE 2. Test rig and flow system.

opening valves B and D and keeping valves A and C closed. Warm water for the buoyant jet discharge is produced by a bank of gas water heaters, with valve B closed and valve A open. The desired flow rate is obtained by adjusting valves C and D and the rotameter valve E. The characteristics of the water heaters require the maximum flow rate to be passed through them, and so the heated water not needed for the jet discharge is allowed to flow through valve C to a dump tank. The warm water, whose flow rate is measured by the rotameters E, is then directed to the plenum chamber shown in figure 3. This has a width of 6 cm. The width of the discharge slot is fixed at 0.6 cm (its length is 30 cm, the width of the test channel), so that the ratio of the contraction between plenum chamber and slot is 10:1.

Within the settling chamber, the water is directed from perforated inlet tubes through perforated plates to the main room of the settling chamber (see figure 3). One further perforated plate was installed in front of the contraction in order to provide good uniformity of the flow and a low exit turbulence level. A dye tube was placed at the beginning of the contraction for injection of dye into the jet. A thermistor was located next to it to record the exit temperature of the jet. Three plastic tubes, called bubble tubes, (marked × in figure 3) were inserted into the settling chamber to remove air bubbles settled there. It should be pointed out that the presence of bubbles caused severe problems and that LDA measurements would have been impossible without removing the bubbles with the aid of the plastic tubes. Large bubbles were sometimes shed from the jet slot in the test channel, making the measurements unreliable. However, small-scale bubbles in the size range 10–50 μm were even more destructive from the measurement point of view because they tended to produce high-quality laser-Doppler bursts, but they were undesirable scattering particles because they moved faster than the fluid due to their high buoyancy. The use of the bubble tubes greatly improved the situation. However, it was found that the bubble generation also depended on the way in which the flow system was set in operation. A very sudden opening of the valves could produce a large amount of
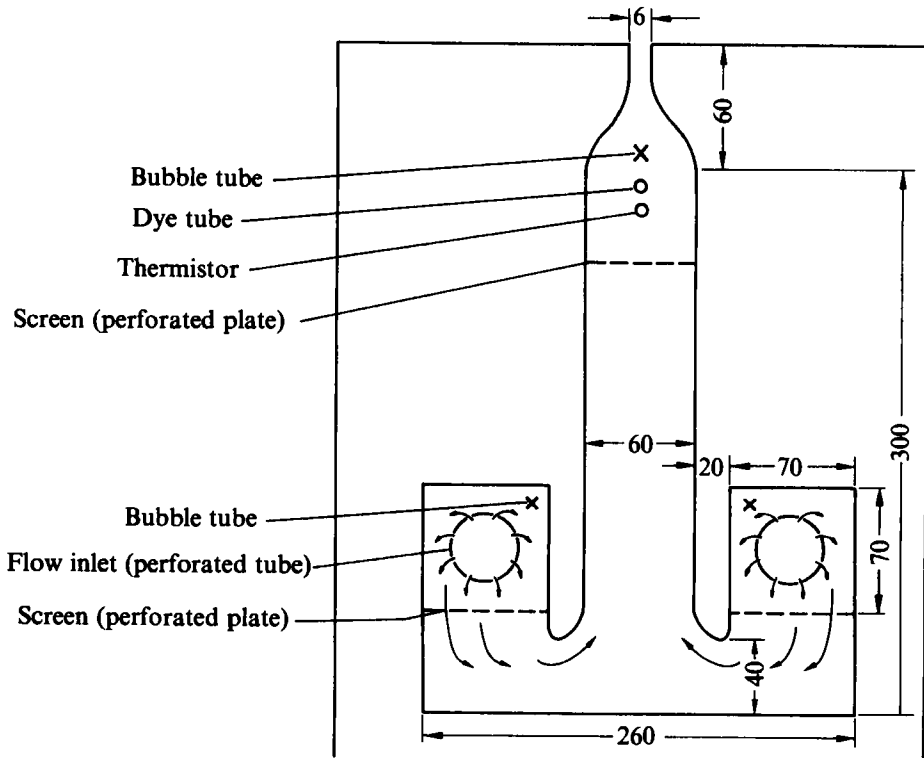
FIGURE 3. Discharge nozzle and settling chamber.

bubbles which could be trapped somewhere inside the plenum chamber and released into the flow in a completely random way.

Two weirs were installed, which could be placed symmetrically with respect to the jet at various distances L_c from the impingement line and could be submerged to various depths d_c (see figure 1 c). The position and depth of the weirs were varied and the final choice of L_c and d_c for the detailed experiments was determined with the aid of flow-visualization experiments as described in §4.

3.2. *Measurement techniques*

Due to rapid variations in the flow direction and the very high turbulence intensities prevailing in the impingement and recirculation regions, reliable velocity measurements are difficult to obtain with the more conventional measurement techniques. Therefore the velocity measurements were taken with a two-channel LDA system (OEI model LD-O-A211) with two Bragg cells for frequency shifting of both channels. This system allows the horizontal and vertical velocity components to be measured independently and detection of the direction of the velocities. Figure 4 shows the basic modules of the optical system which consists of a Spectra Physics Argon Ion two-colour laser source of 2 W total power, beam-returning unit, beam-splitter module with colour filter, back-scattering module, lens module and two photomultipliers. The distance of the interference fringes was 3 µm for the blue beam ($\lambda = 488$ nm) and 3.18 µm for the green beam ($\lambda = 514.5$ nm). Every effort has been made to focus the two control volumes for the individual colour beams on the same point. However, complete coincidence could not be achieved. Only about 60–80 % of the total number of bursts took place simultaneously at both channels. The outputs of both photo-
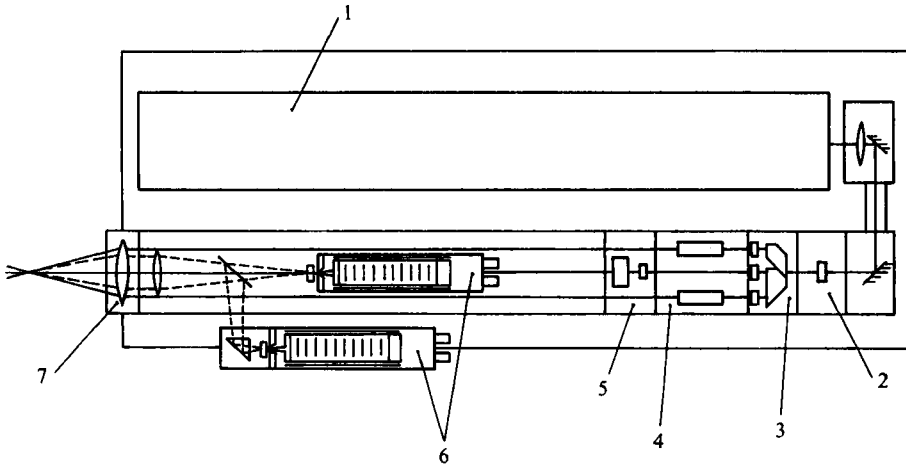
FIGURE 4. Arrangement of the LDA optics: 1, laser source; 2, polarization module; 3, beam splitter; 4, Bragg cells; 5, beam-splitter and polarization module; 6, photomultipliers; 7, focusing lens.
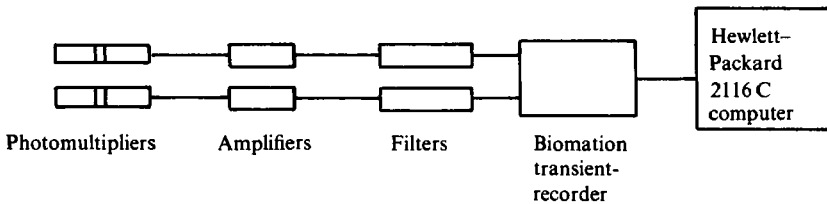

FIGURE 5. Block diagram of equipment for data acquisition and digital processing of laser-Doppler bursts.

multipliers were amplified and filtered using OEI variable band-pass filters of model LD-E310 and were finally fed to a Biomation transient recorder which digitized the actual *burst signal* and then transferred the data to a Hewlett–Packard computer model HP 2116C for further digital processing (see figure 5). The transient recorder, which had a 8-bit resolution, was triggered to acquire and transfer data only when a burst was present at *both* channels.

The LDA system was operated in the back-scattering mode. As the intensity of the scattered light is orders of magnitude weaker in this mode than when the operation is in the forward-scattering mode (see Durst, Melling & Whitelaw 1981) the resulting signal to noise ratio (SNR) is rather low. Owing to the low SNR, the usual zero-crossing counter technique of Durst & Tropea (1977) for determining the Doppler frequency of a single burst was found to be rather erratic. Therefore, a new technique was developed which determines the bursting frequency from the frequency spectra constructed from the digitized data of the individual bursts with the aid of fast Fourier transforms (FFT). This technique is described in the Appendix. The time required to process one burst at both channels was of the order of 2 s. 3000–4000 bursts was required to obtain statistical averages. Thus the total measurement time for one experimental point was of the order of 2 h.

In the buoyant situation, difficulties arose in the LDA measurements due to the refractive-index fluctuations caused by the temperature fluctuations in the flow. The refractive-index fluctuations not only led to uncertainties in the position of the intersection point of the beams but also caused spurious results in regions where the

mean-flow velocities were very small. This is because the laser technique measures the velocity of seeding particles relative to the fringe pattern. Thus if the fringe pattern fluctuates due to the refraction of the beams taking place at a warm–cold water interphase, which may be far from the measuring point, the measured velocity is non-zero even when the seeding-particle velocity in the measurement point is zero. If we assume, for example, that the control volume oscillates with a frequency of 10 Hz, which is roughly the frequency of the appearance of the large structures in the jet, and with an amplitude of the order of $A = 200$ μm, then it follows that the measured velocity $U = 2\pi f A \cos 2\pi f t = U_0 \cos 2\pi f t$, where $U_0 = 1.8$ cm/s. It is obvious that such high values of the velocity amplitude U_0 can cause unacceptable errors in the measurements of turbulent quantities. This problem, which affects mainly the horizontal beams measuring the horizontal velocity component U, virtually disappears when the local temperature difference between the jet and ambient fluid is less than 7 °C. Results that may be affected by refractive-index fluctuations are not included in the presentation of the velocity measurements below. In certain situations, the flow needed to be seeded, and fine TiO_2 particles of 1–2 μm diameter were used for this purpose. A solution containing these particles was fed into the system via one of the bubble tubes.

The mean temperature field was measured with a rake of thermistors. The flow-visualization studies were performed by injecting dye continuously into the plenum chamber. Checks on the two-dimensionality of the flow were made by measuring the spanwise velocity and excess temperature distribution near the surface in the near field. The distributions were found to be uniform (to within 1–2 % of their discharge values) over at least 80 % of the channel width. Hence there should be no significant three-dimensional effects in the middle portion; the measurements reported in §5 were taken at the middle plane.

4. Flow-visualization studies

The flow-visualization experiments served two purposes: to identify the geometrical and discharge parameters for which a stable flow is established with a complete roller occurring in the test section; and to obtain and record information on the global flow behaviour and its dependence on the various parameters. The effects of the following four parameters were studied in the visualization experiments:

(a) the Froude number F, which was adjusted by varying the flow rate and the temperature difference $\Delta T = T_0 - T_a$;

(b) the ratio of water depth to discharge width H/B, by varying the water depth H;

(c) the distance of the downstream control weir from the jet centreline L_c;

(d) the submergence of the control weir d_c.

When dye is injected into the discharge jet it is convected along with the fluid and at the same time diluted by mixing with the ambient water. In the initial period after the start of the injection, the dye picture is mainly governed by convection processes except in the vertical jet itself where rapid mixing takes place. In the other part of the flow mixing is much slower, particularly in regions with strong stratification, and it takes quite a while before the dye concentration approaches a steady-state distribution. It is because of this relative lack of mixing that the motion of the dyed fluid can be observed fairly well in the initial period. Unfortunately, this motion cannot be captured by photographs but can only be observed by eye (or captured with the aid of a movie camera). At a later stage, when diffusion processes had sufficient time to be effective, the dye is fairly well mixed in the warm-water layer,
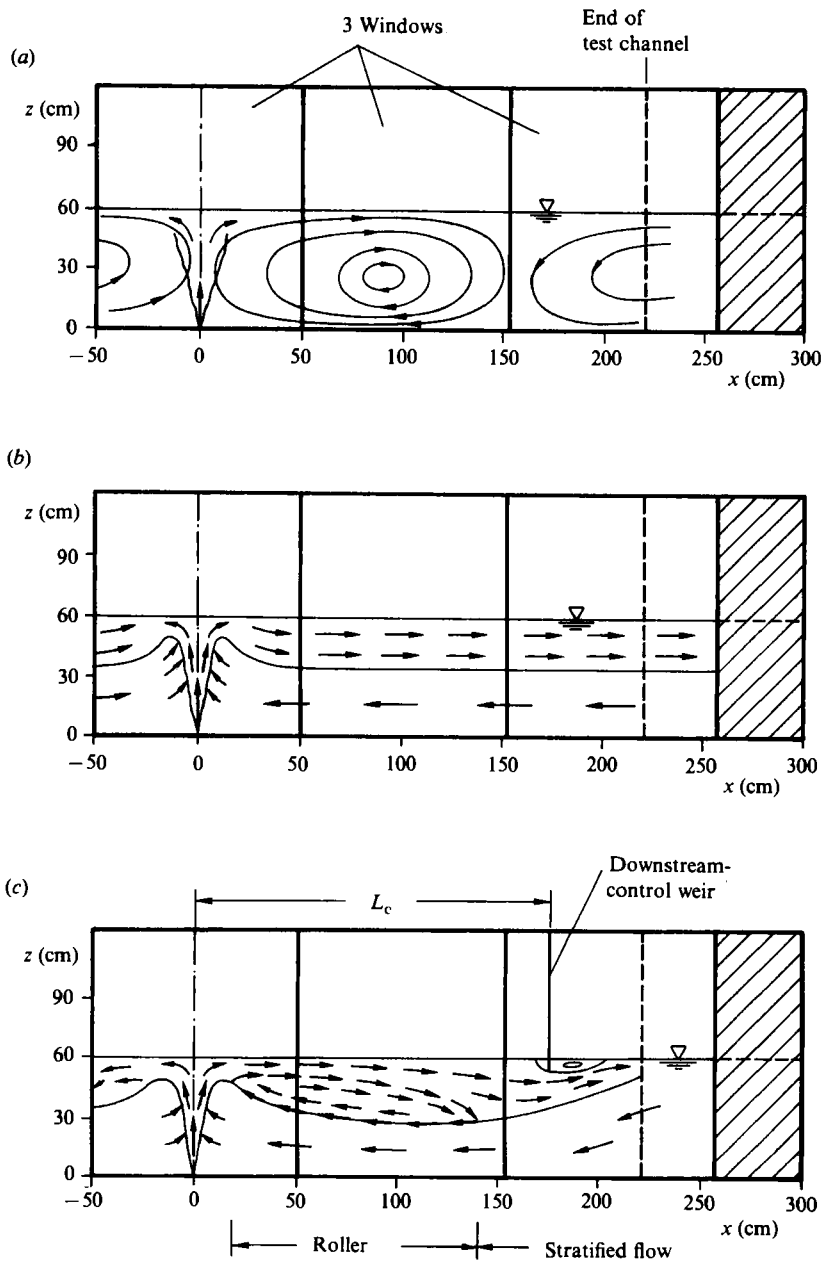
FIGURE 6(*a–c*). For caption see facing page.

and the picture is now much less informative. The motions can now no longer be discerned but only the thickness of the dyed layer.

In the visualization experiments the following procedure was adopted. Start-up dye studies were performed in order to obtain information on the establishment of the flow field and in particular on the presence of a roller in the stratified counterflow. In these studies, the flow was first allowed to develop without dye injection. The dye
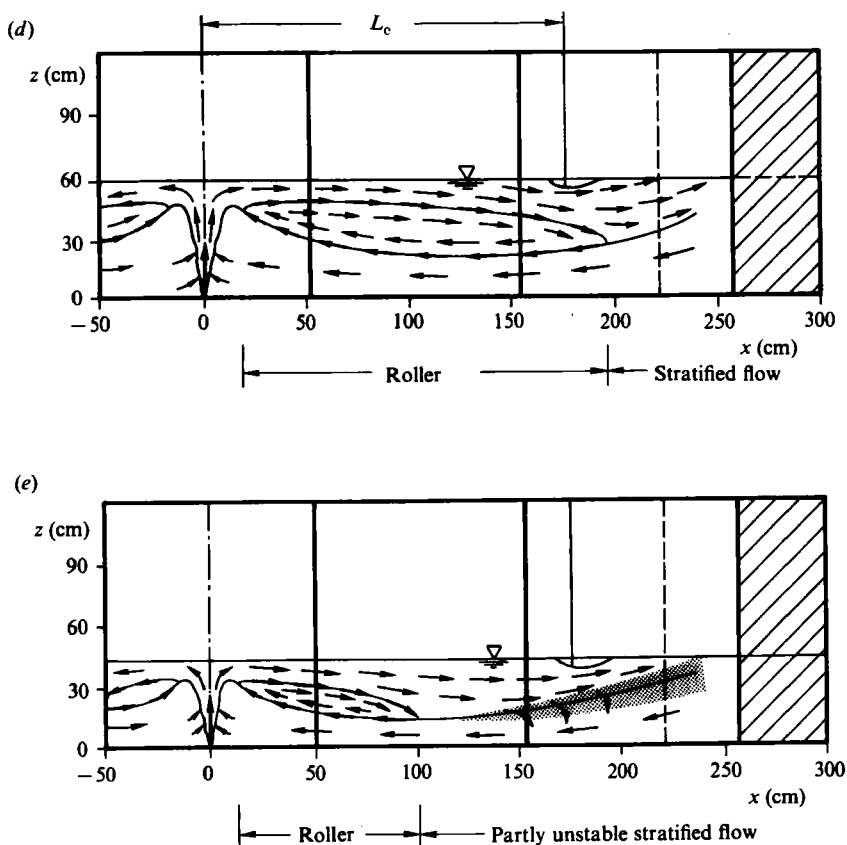
FIGURE 6. Flow situations sketched from observations by eye: (a) Non-buoyant flow, $F = \infty$, $Re = 1318$, $H/B = 1008$; (b) $F = 12$, $Re = 2635$, $H/B = 100.8$, no downstream control; (c) Parameters as in (b), but with strong downstream control: $L_c = 175$ cm, $d_c = 5$ cm; (d) $F = 25.3$, $Re = 5200$, $H/B = 100.8$ with strong downstream control: $L_c = 175$ cm, $d_c = 5$ cm; (e) $F = 9.7$, $Re = 2635$, $H/B = 75.8$ with strong downstream control: $L_c = 175$ cm, $d_c = 5$ cm.

injection was then started and the movement of the dyed fluid elements was observed. In the initial period before mixing became effective, the flow pattern was visible and a roller could clearly be identified in certain parameter situations; in particular, the point could be located where the roller ended and the fluid turned round. However, the motion does not show on photographs and could only be observed by eye by following individual clouds of dye. The visual impression is sketched in figure 6 for a number of parameter situations. It should be remembered that these sketches do not represent steady-state dye pictures so that differences to pictures taken much later after the start of the dye injection must be expected.

Photographs have been taken at various times after the start of the dye release and are shown in figures 7–11. Most pictures were taken after a considerable time had elapsed in which mixing took place and a situation approaching the steady state prevailed. As already mentioned, these photographs mainly provide information on the thickness of the dyed layer. Unfortunately, it is not entirely clear what the visible edge of the dyed layer represents and hence a direct comparison with the measured temperature field is somewhat difficult.

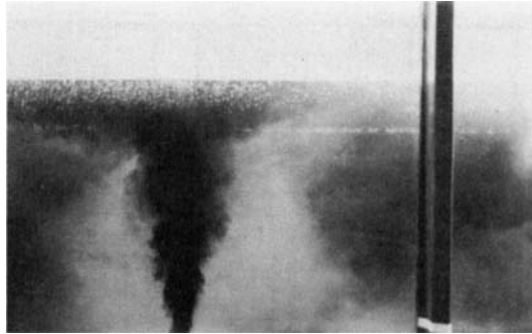One of the main objectives of the visualization study was to establish the effects

FIGURE 7. Flow visualization for $F = \infty$, $Re = 1318$, $H/B = 100.8$, $t = 7$ min.

of the downstream-control weir. First, non-buoyant flows ($F = \infty$) were investigated. In these cases, the positioning of a submerged weir near the end of the test channel had no effect on the overall flow pattern for the relatively small submergence depths d_c/H studied. For $H/B \approx 100$, the observed flow pattern is sketched in figure 6 (a) and can be seen to be in accord with the pattern observed in previous investigations (see §2). A primary recirculation zone is established which occupies virtually the whole depth and extends to about $2.5H$ downstream. Part of a secondary zone could also be observed as sketched in figure 6 (a). A photograph of this flow is given in figure 7. The picture covers only half of the primary cell. The dye can be seen to be distributed over the full depth of the test channel so that clearly an unstable situation exists with dye being recirculated and re-entrained into the jet. It should be added that the recirculating motion was observed in all the visualization experiments, including some with dye injection at the surface. Even though each experiment gives only an instantaneous picture, the sum of them confirms the presence of a steady-state recirculation.

For the same $H/B (\approx 100)$, buoyant discharges are now considered. Figure 6 (b) shows the flow pattern observed for a situation with $F = 12$ and without a downstream-control weir. In this case, no roller could be observed in the test section. Over most of the section, there appeared to be a stratified counterflow with the two layers of nearly constant depth. After the impingement region, there was a fairly rapid increase in the thickness of the upper layer. This suggests the presence of an internal hydraulic jump, but the existence of such a jump could not be identified with certainty. When a weir with relative submergence $d_c/H = \frac{1}{12}$ was placed as downstream control near the end of the test channel (all other conditions remained the same), a different flow pattern developed in which a roller could clearly be identified as sketched in figure 6 (c). This roller ended before the downstream control weir, and the length of the roller region is of the order of $2H$. This corresponds to the figure quoted by JH. The depth of the warm-water layer is now larger than in the case without a control weir, but this depth decreases in the stratified counterflow region beyond the roller as indicated in figure 6 (c). In figure 6 (d) the flow pattern observed for a Froude number twice as high ($F = 25.25$) is sketched. The increase in Froude number seems to make the internal hydraulic jump stronger, as the roller region is now longer ($\approx 2.8H$) and extends beyond the control weir. The roller region is also thicker and so is the entire warm-water layer. This increase in conjugate depth of the layer after the jump with Froude number is in general accord with the analysis of JH.

Initial tests with variable locations L_c of the control weir have shown that, because at $H/B \approx 100$ the length of the roller is more than half of that of the test section, the weir must be placed close to the end of the test channel if a complete roller is to be established in this channel. However, the flow should be allowed to develop over some distance beyond the weir in order to facilitate the specification of downstream boundary conditions in numerical calculations. Hence, the weir was placed 45 cm from the end of the test channel. The submergence of the weir d_c has to be larger than a critical value in order to trip the establishment of a hydraulic jump associated with a clearly visible roller. As will be shown below, the resulting jump is always flooded because of the comparatively large length of the roller. Consequently, the upper layer is quite thick and there is a tendency for this layer to reach the ground and for the flow to become unstable when the submergence d_c is increased much further. A submergence of $d_c = 5$ cm was chosen, which is safely beyond the critical value for all parameter situations but at the same time allows the realization of stable situations, at least at lower Froude numbers.

Photographs of buoyant flows very similar to those just discussed are given in figures 8 ($F = 9.9$) and 9 ($F = 21$). For these two cases, pictures are presented for various times after the start of the dye injection, the last photograph in each series representing a state where the dye picture no longer changed noticeably. In figure 9(a), the dye has just reached the surface and starts to spread sideways while in figure 8(a) this spreading is already in progress, the downward component of the velocity after deflection (see figures 6c and 22) causing the apparent thickening of the jet in the near-surface region. Figures 8(b) and 9(b) show the development of the dye pictures at intermediate times. Here the rapid thickening of the warm-water layer, indicating an internal hydraulic jump, is apparent, and also the interaction of this jump with the jet, indicating the flooded nature of the jump. A further intermediate picture is included as figure 9(c) which is already fairly close to the 'steady-state' picture in figure 9(d), but clearly shows that the depth of the upper warm-water layer is still increasing slowly.

From the last picture in each series one can observe that the depth of the warm-water layer and hence the conjugate depth of the internal hydraulic jump increases with the Froude number. These photographs are for a much later time after the dye injection started than the flow sketches in figures 6(b and d) so that the dyed layers are thicker; in the case of $F = 21$ the dyed layer almost reaches the bottom, indicating that this case is at the verge of instability. This notion is consistent with the fact that the jump can be seen from the photographs to be flooded. Both pictures show a rather thick dyed layer in the vicinity of the jet, indicating that the roller is not separated from the jet and does not entrain ambient water in the upper part but re-entrains dyed water. The picture is typical for a flooded jump, and this finding will be confirmed further by the temperature measurements presented below. This phenomenon was not observed in the start-up studies which formed the basis for the sketches of figure 6. The reason is simply that time was too short for the dye to fill the near-jet upper region. It should further be noted that the photographs in figures 8(c) and 9(d) cover only the range up to $2.2H$ and therefore do not include the end of the roller region and the stratified counterflow region.

A number of experiments were carried out to investigate the influence of the relative depth H/B. Figure 6(e) shows the flow pattern as observed for smaller relative depths than in the previous cases ($H/B \approx 75$) for a Froude number $F = 9.7$. The roller region is now clearly shorter than in the case sketched in figure 6(c), which is the closest situation at the larger water depth. However, the ratio of roller length
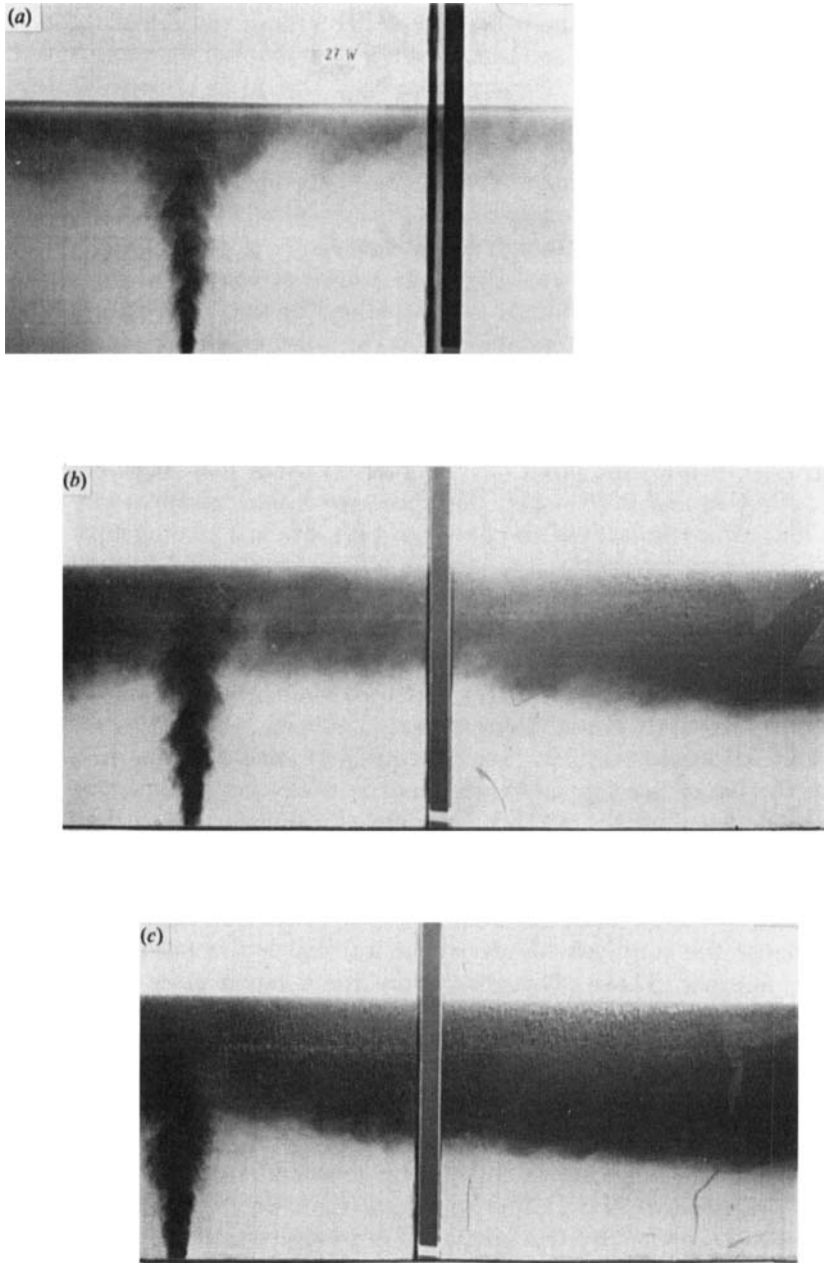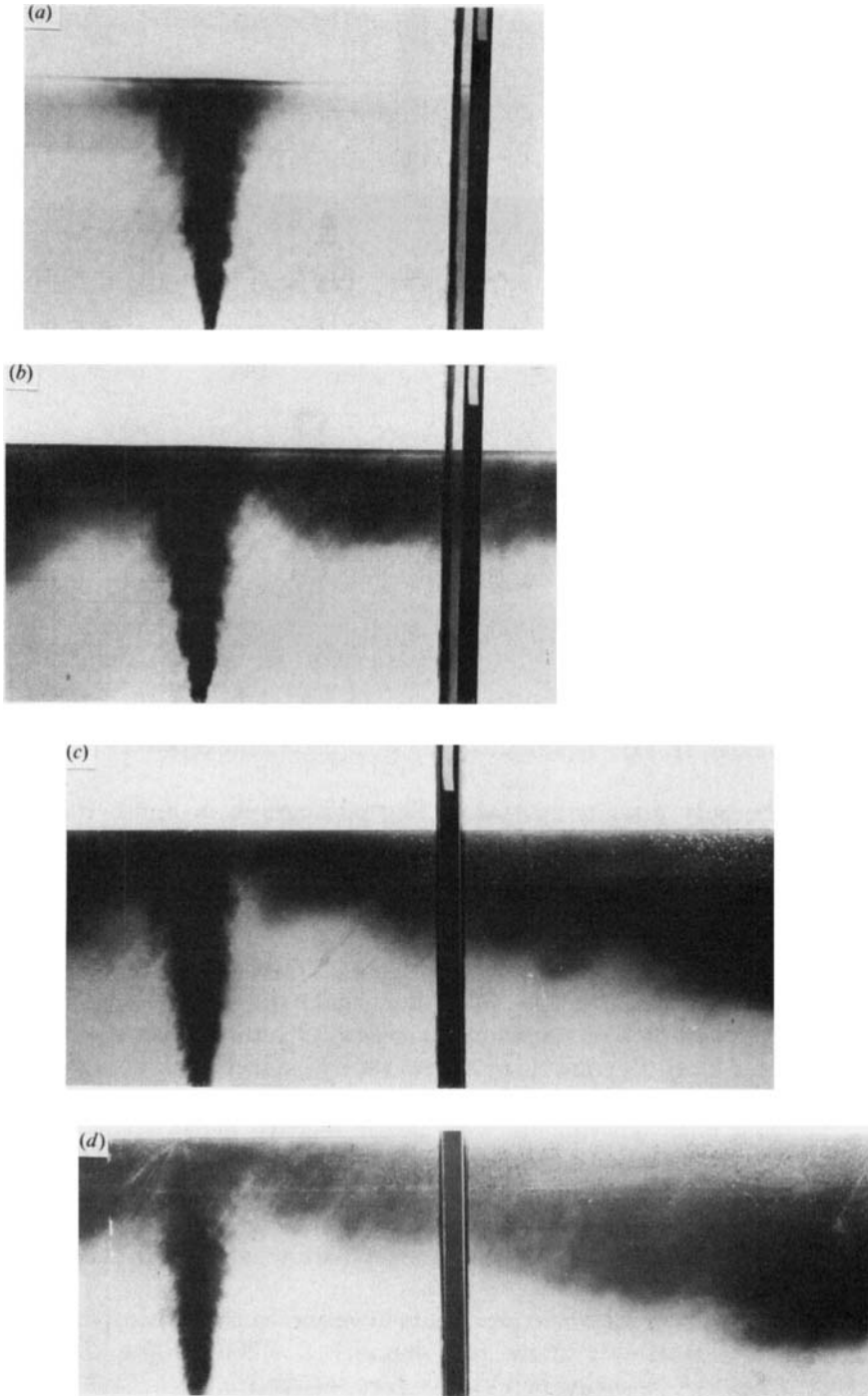
FIGURE 8. Flow visualization for $F = 9.9$, $Re = 2635$, $H/B = 100.8$, $d_c/H = \frac{1}{12}$:
(a) $t = 5$ min, (b) 15 min, (c) 30 min.

to water depth is about the same, namely $2H$. The layer depth after the jump and hence the conjugate depth, relative to the water depth H, is larger than in the case of figure 6(c) with higher H/B. This trend is again in agreement with the JH analysis. As the upper layer is now fairly close to the bottom, there is a tendency to flow instability and to interaction between the upper layer and the ambient flow. Hence no clear-cut stratified counterflow could be observed in this case, which must be

FIGURE 9. Flow visualization for $F = 21$, $Re = 5197$, $H/B = 100.8$, $d_c/H = \frac{1}{12}$: (a) $t = 1$ min, (b) 3 min, (c) 20 min, (d) 30 min.
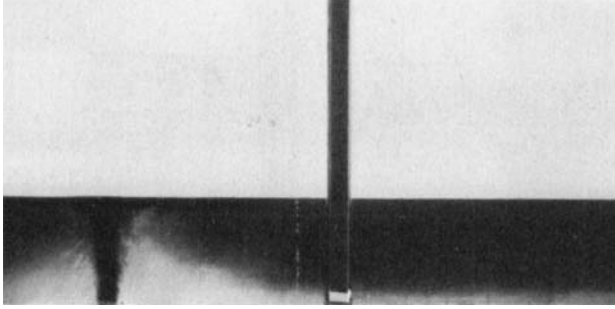
FIGURE 10. Flow visualization for $F = 9.7$, $Re = 2635$, $H/B = 50$, $d_c/H = \frac{1}{12}$.
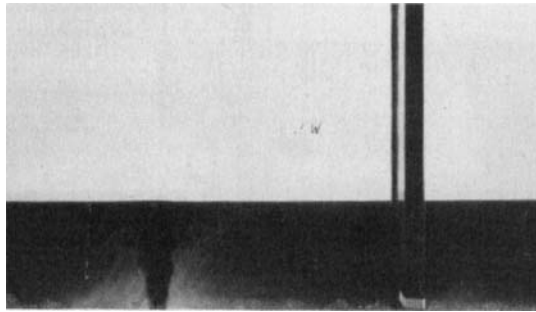

FIGURE 11. Flow visualization for $F = \infty$, $Re = 2675$, $H/B = 50$.

considered to be only marginally stable. The photograph in figure 10 presents a picture for an even smaller relative depth, $H/B = 50$, for the same Froude number of 9.7. This picture also shows a large depth of the warm-water layer, extending nearly to the bottom. The picture covers a downstream distance of roughly $3H$ and thus includes the roller region: it also indicates the presence of a flooded jump.

As a contrast, figure 11 shows, for the same H/B ratio, non-buoyant discharge, which is clearly unstable. The dye filled the whole test channel, and a primary recirculation zone can be seen as being represented by the darker dye. This again extends to roughly $2.5H$. Beyond this distance the dye, which must be associated with the secondary zone, is somewhat fainter.

In the buoyant-flow experiments with larger relative depth ($H/B = 125.8$ and 175.8) the flow pattern was qualitatively similar to that in figure 6(b), i.e. a roller was not observed in the test channel. However, a stable flow with fairly rapid increase of the thickness of the dye layer beyond jet impingement was observed in all cases except those at very high Froude numbers, possibly indicating the presence of hydraulic jumps.

In summary, the visualization experiments have shown that a complete roller was established in the relatively short test channel $L = 200$ cm (i.e. $L = 3.3H$ for $H/B = 100$), when the following conditions were satisfied:

(i) A strong downstream control was imposed near the end of the test section (sharp control weir with sufficient submergence; $d_c/H = \frac{1}{12}$ was found adequate);

(ii) the water depth H was less than $\frac{1}{3}$ of the length of the test channel which is $L = 200$ cm. Therefore $H < 70$ cm, i.e. $H/B < 116$; and

(iii) the densimetric Froude number was low, say $F < 30$.

Since the tendency of a stable flow to break down into an unstable one increases as the relative depth decreases, the detailed measurements in a stable flow reported in the next section were taken at $H/B \approx 100$. For that depth, the visualization experiments for the Froude-number range 10–12 clearly indicate a stable flow (see figures 6c and 8). At this point it is of interest to compare the observations with the JH analysis. This predicts a stable situation when the stability parameter $F(H/B)^{-\frac{3}{4}}$ is below 0.63 and an unstable one when it is above, at least for large H/B-values, say $H/B > 50$. For smaller H/B-values, the finite source effects become important and the theory deviates from this criterion (see figure 9 of JH). For $H/B \approx 100$ and F in the range 10–12, the stability parameter assumes values of 0.31–0.37, so that the observed stable nature of the flow is in agreement with the JH stability analysis. On the other hand, the stability parameter for the Froude-number range 21–25 (again for $H/B = 100$) is 0.66–0.78 so that, according to the stability analysis, the flow should be unstable, but very close to the border between stable and unstable. The visualization experiments for these Froude numbers displayed in figures 6(d) and 9 indicate that the flow is still stable, but from the photographs in figure 9 a tendency to instability is clearly visible. Hence there is no gross disagreement with the stability diagram of JH. It should be noted that the strong downstream control imposed in the present experiments, which was absent in JH's experiments and analysis, can be expected to have a considerable influence on the limiting Froude number at which a stable flow breaks down into an unstable one. Keeping this in mind, the findings of the flow-visualization studies are in fairly good agreement with the JH stability analysis.

5. Detailed measurements

For the actual flow measurements, parameter ranges were chosen that, according to the visualization studies, are in the unstable range on the one hand and the stable range on the other. The unstable experiments were carried out for a non-buoyant jet discharge ($F = \infty$) at two different Reynolds numbers; in order to get a stable situation with a complete roller in the test section, experiments had to be carried out at relative depths $H/B < 110$ and $F < 25$. Most experiments (both for unstable and stable situations) were carried out for $H/B = 100.8$ and the other parameters for this depth are given in table 1. A few results will be included also for smaller and larger depths.

5.1. *Jet region*

Experimental results will be presented first for the vertical jet region, starting with velocity measurements for the non-buoyant cases ($F = \infty$). Figure 12 shows the mean velocity profiles for the water depth $H/B = 100.8$ and the two Reynolds numbers 2635 and 5197 in the dimensionless form W/W_M versus $\eta = x/(z-z_0)$, where W_M is the maximum velocity at the jet centreline and z_0 is the virtual origin of the jet. Profiles are included at different z-locations far from the initial region but excluding the impingement region near the free surface. The virtual origin has been determined by extrapolating the half-width development determined from velocity profiles at various z-locations to the zero location. The data show that, at least in the region considered, the jet is self-preserving and spreads linearly and that the self-similar velocity profiles follow closely the Gaussian distribution

$$\frac{W}{W_M} = \exp\left(-k_u \eta^2\right),$$

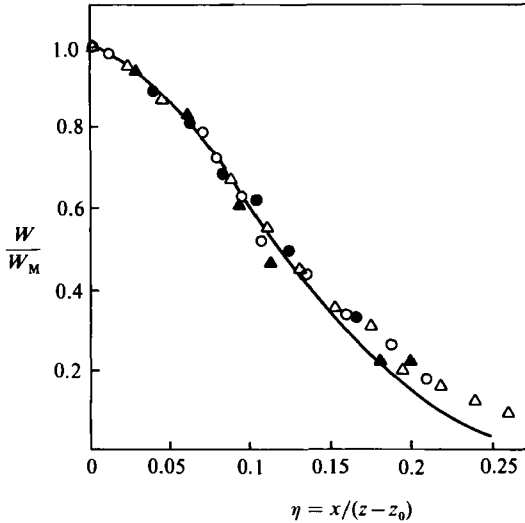| W_0 (cm/s)	T_a (°C)	T_0	F	$Re = W_0 B/\nu$	
25.1	12.4	48.4	9.9	2635 ⎫	Buoyant cases
50.2	16.2	47.6	21	5197 ⎭	with $d_c/H = \frac{1}{12}$
25.1	15	15	∞	1318 ⎫	Non-buoyant
50.2	15	15	∞	2637 ⎭	cases

TABLE 1. Flow parameters for studies at $H/B = 100.8$

FIGURE 12. Mean-velocity distribution in the free-jet region for the non-buoyant case: $F = \infty$, $H/B = 100.8$. $Re = 5197$: $\triangle$, $(z-z_0)/B = 45$; $\bigcirc$, $(z-z_0)/B = 67$. $Re = 2635$: $\blacktriangle$, $(z-z_0)/B = 55$; $\bullet$, $(z-z_0)/B = 80$.

with the coefficient $k_u = 50$. There is only a small difference in the self-similar profiles between the two Reynolds numbers. In their review of experimental data, Chen & Rodi (1980) recommend a value of $k_u = 62$, which implies a 10% smaller spreading rate. The larger jet spreading in the present experiments, and also the fact that the velocities are somewhat higher than the Gaussian profile near the edge, is most likely caused by the fact that the ambient flow régime is not at rest and that it carries a fairly high turbulence, as can be seen from figure 7 and also more quantitatively from figures 13 (*a, b, c*) which display, for the non-buoyant situations the measured stresses $\overline{w^2}$, $\overline{u^2}$ and $\overline{uw}$ respectively, made dimensionless with the centreline velocity W_M. Figures 13 (*a, b*) indicate that there seems to be a marked influence of the Reynolds number on the relative normal stresses, and it is clearly noticeable that these have fairly high values at the edge of the jet, in particular in the case of the lower Reynolds number. This may also be responsible for the fact that the normal stress profiles at different locations are not in general self-similar. It is interesting to note that, in the edge region, the two stresses have roughly the same level. This, in connection with the observation that the shear stress $\overline{uw}$ is small at the edge and in the ambient, allows the conclusion that the turbulence is fairly isotropic in the recirculation zone outside the jet. The shear-stress data in figure 13 (*c*) show much better self-preservation, and the measurements can also be seen to follow quite well the shear-stress distribution
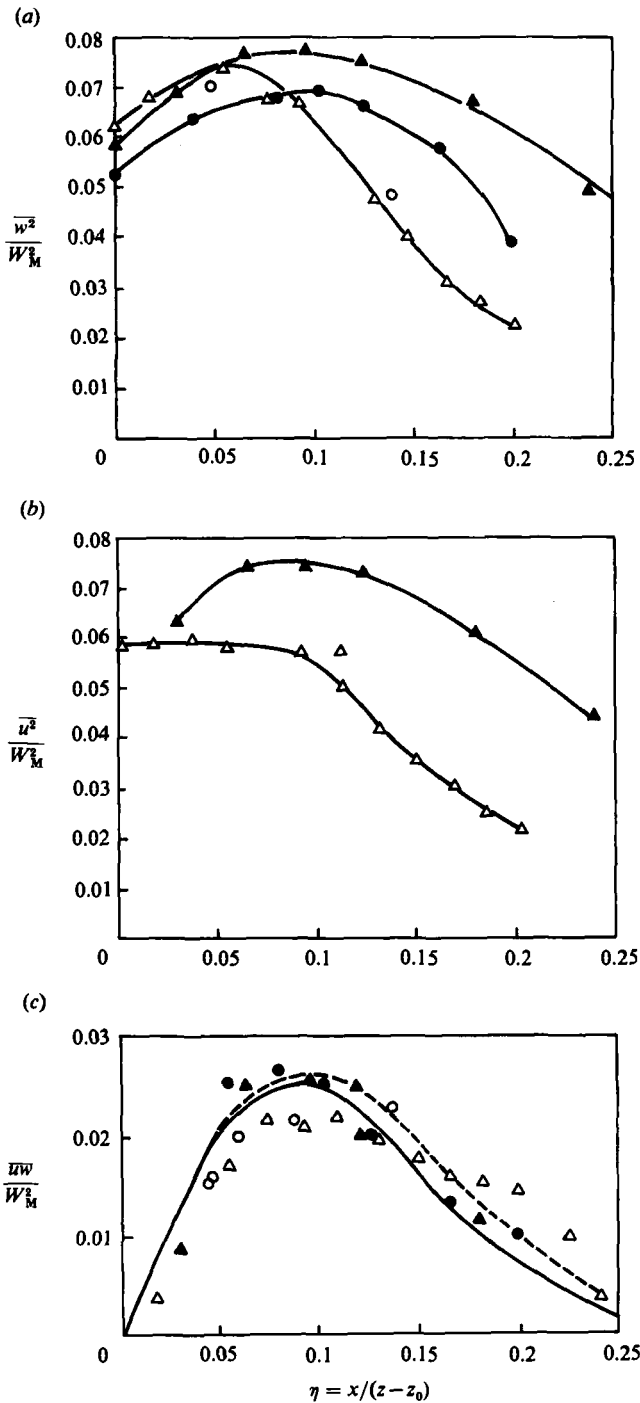
FIGURE 13. Turbulent stress distributions in free-jet region for non-buoyant case: $F = \infty$, $H/B = 100.8$. ●, $(z-z_0)/B = 80$, $Re = 2635$; ▲, $(z-z_0)/B = 55$, $Re = 2635$; ○, $(z-z_0)/B = 67$, $Re = 5197$; △, $(z-z_0)/B = 45$; $Re = 5197$. (a) longitudinal fluctuations $\overline{w^2}$; (b) lateral fluctuations $\overline{u^2}$; (c) shear stress $\overline{uw}$; self-similar distribution determined from mean velocity via momentum equation: ——, $Re = 2635$; ————, $Re = 5197$.
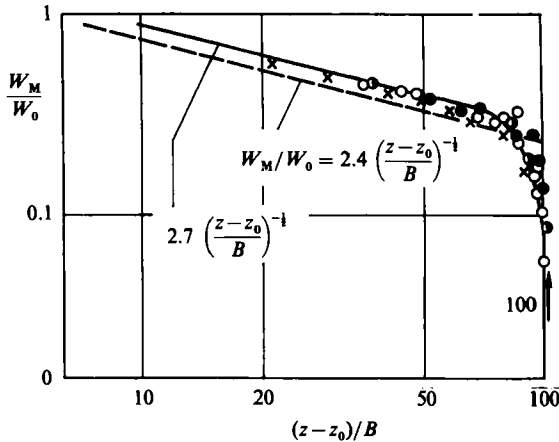
FIGURE 14. Decay of centreline velocity; present data for $H/B = 100.8$: $\bigcirc$, $F = 21$, $Re = 5197$; $\bullet$, $F = 9.9$, $Re = 2673$; $\mathbb{O}$, $F = \infty$, $Re = 2637$; $\times$, Gutmark et al.'s (1976) data for a jet impinging on wall.

obtained via the momentum equation from the mean velocity profiles. This proves the consistency of the mean-velocity and turbulence measurements.

The decay of the mean velocity at the jet centreline W_M made dimensionless with the exit velocity W_0, is plotted in figure 14 for various experimental conditions, now including buoyant-jet situations. Further, the impingement region is included. In free jets, the centreline velocity is known to obey the following decay law:

$$\frac{W_M}{W_0} = C_u \left(\frac{z - z_0}{B}\right)^{-\frac{1}{2}}.$$

In their review of experimental data, Chen & Rodi (1980) recommended a value of 2.4 for the decay constant C_u, while Tennekes & Lumley (1972) recommend a value of 2.7. The decay lines according to both laws are included in figure 14, and it can be seen that the present measurements correspond initially very closely to the decay law with $C_u = 2.7$. Close to the free surface, indicated by an arrow, the velocity drops to zero very rapidly. For the non-buoyant and moderately buoyant cases, there is good agreement with the data of Gutmark, Wolfshtein & Wygnanski (1976)† for a jet impinging on a wall, also at a relative distance of $H/B = 100$. This supports the notion that jets impinging on a free surface and on a wall do indeed behave rather similarly. For the situation with fairly strong buoyancy, $F = 9.9$, the centreline velocity appears to start its sharp decay closer to the surface than in the cases with zero buoyancy. In order to examine the influence of the buoyancy, the centreline velocity decay is replotted in figure 15 according to the scaling law of Chen & Rodi (1980) in which both W_M/W_0 and the relative distance z/B are multiplied by appropriate exponential functions of the densimetric Froude number F. In this way of plotting, the velocity decay in jets follows a single curve for the whole range between non-buoyant and strongly buoyant jets (pure plumes). Also, from the decay behaviour three regions can be identified, namely a non-buoyant region, an intermediate region and a pure-plume region as shown in figure 15. In this figure,

† This original report is referred to instead of the later publication (Gutmark, Wolfshtein & Wygnanski 1978) because the latter involves some error in the presentation of the centreline velocity data.
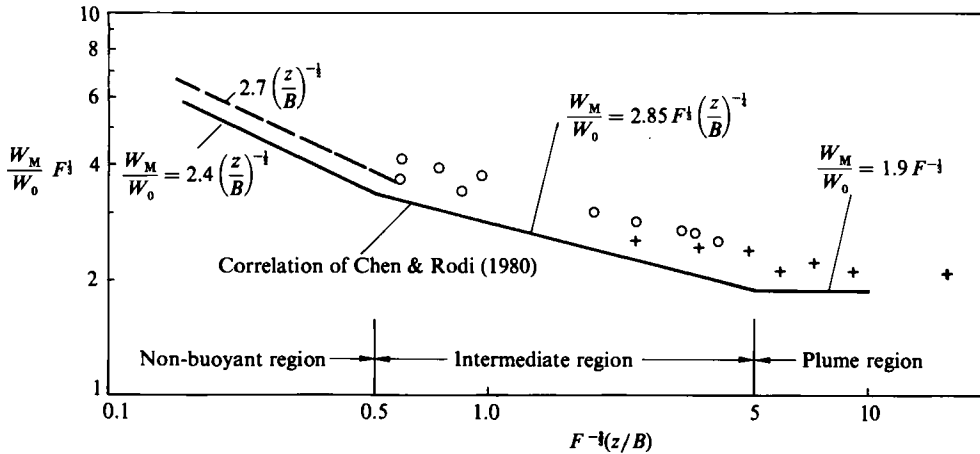
FIGURE 15. Decay of centreline velocity: $\bigcirc$, present results; $+$, Ramaprian & Chandrasekhara (1983).

the present measurements (excluding the data in the impingement region) are compared with Chen & Rodi's (1980) correlation. The data for the case with $F = 21$ can be seen to fall into the beginning of the intermediate region; they still follow roughly the $-\frac{1}{2}$-decay law prevailing in the non-buoyant region. On the other hand, the data for the case with $F = 9.9$ are more towards the end of the intermediate region and follow roughly the $-\frac{1}{4}$-decay law suggested by Chen & Rodi (1980) for this region. The data are however consistently higher than the correlation. Ramaprian & Chandrasekhara's (1983) recent measurements are also included in the figure; they extend from the intermediate region into the pure-plume region and lie between the present measurements and the Chen & Rodi (1980) correlation. The fact that the present data lie above the correlation may again be because the ambient is not at rest in the present case and a flooded hydraulic jump involving a roller is present at the edge of the jet in its upper part. In general, however, the measurements can be seen to follow quite well the established trends of buoyant-jet behaviour.

Corresponding results are now presented for the excess temperature. Figure 16(*a, b*) respectively show, for $F = 9.9$ and 21, the streamwise development of the horizontal excess temperature profiles in the jet region non-dimensionalized by the local centreline value, $\Delta T_{M} = T_{M} - T_{a}$. In both cases, the two profiles closest to the discharge appear to follow the Gaussian distribution

$$\frac{\Delta T}{\Delta T_{M}} = \exp\left(-k_{c}\,\eta^{2}\right),$$

with $k_{c} = 41$ and 45 for $F = 21$ and 9.9 respectively. These values compare with $k_{c} = 35$ and 50 recommended for plane pure jets and pure plumes respectively in Chen & Rodi's (1980) review. Considering the fact that the two Froude-number cases investigated fall into the intermediate-to-plume ranges according to figure 15, the agreement is quite good. At distances $(z - z_{0})/B$ larger than about 25, departures from the Gaussian similarity profile can be observed that are due to the fact that the temperature outside the jet is no longer at its ambient value T_{a}. The increase in outside temperature at relatively low heights is caused by the presence of a submerged jump interacting with the jet. This increase is illustrated more directly by the vertical
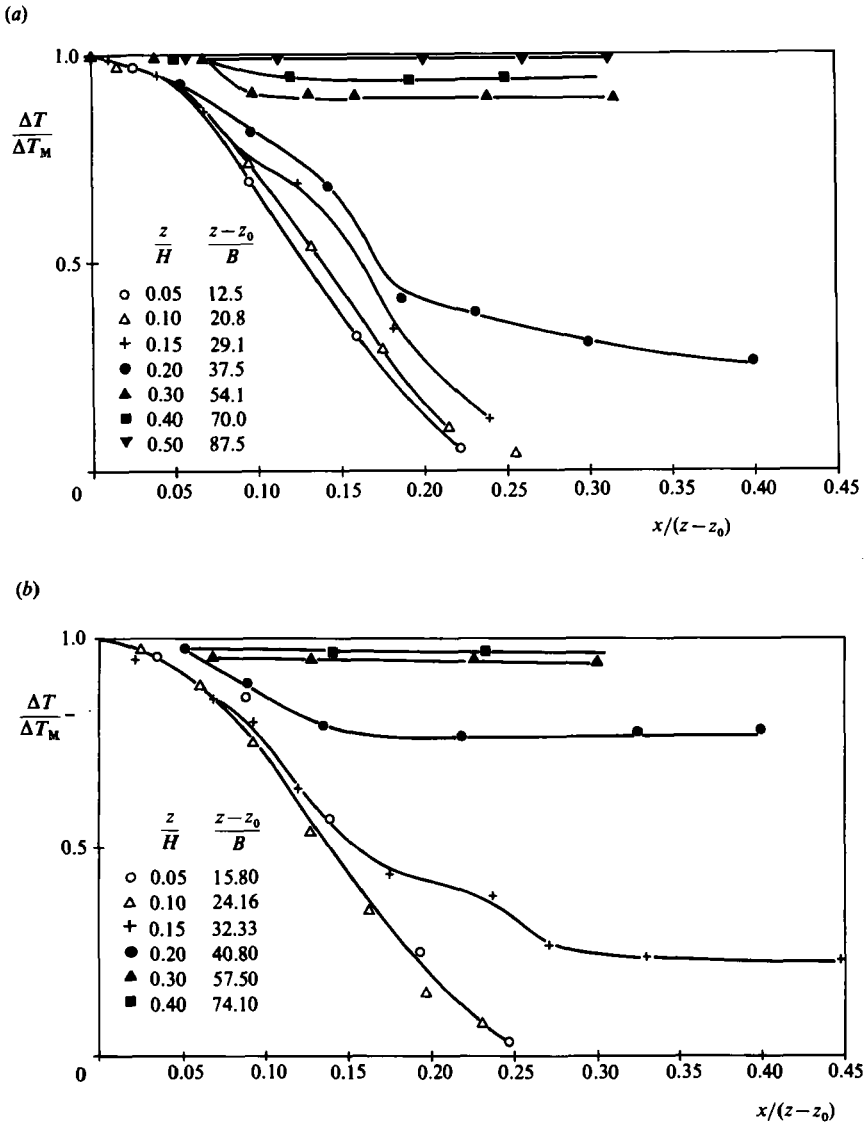
FIGURE 16. Horizontal temperature profiles in the jet and its surroundings: (a) $F = 9.9$, $H/B = 100.8$, $Re = 2635$; (b) $F = 21$, $H/B = 100.8$, $Re = 5197$.

temperature profiles presented below in figure 20. The horizontal profiles in figure 16 show clearly that the temperature is fairly constant and the same as outside the jet in the upper part. The evolution of the temperature field is very similar in both Froude-number cases, the increase in outside temperature occurring somewhat earlier for $F = 21$ because the upper heated layer is thicker in this case (see figure 20).

In figure 17 the decay of the excess temperature is plotted for discharges into two depths and at the two Froude numbers 9.9 and 21 in each case. The position of the free surface is again indicated by arrows in the figure. In non-buoyant jets, the decay of the centreline excess temperature is known to follow the law

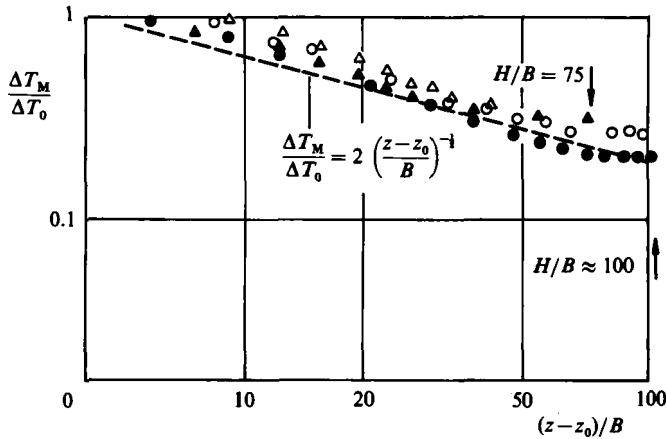$$\frac{\Delta T_M}{\Delta T_0} = \frac{T_M - T_a}{T_0 - T_a} = C_T \left(\frac{z - z_0}{B}\right)^{-\frac{1}{2}}.$$

FIGURE 17. Centreline excess-temperature decay: $F = 9.9$, $Re = 2635$: $\bullet$, $H/B = 100.8$, $\blacktriangle$, $H/B = 75$. $F = 21$, $Re = 5197$: $\bigcirc$, $H/B = 100.8$, $\triangle$, $H/B = 75$.

In their review of experimental data Chen & Rodi (1980) have recommended a value of 2 for the decay constant $C_{\rm T}$. The decay law with this constant is included in figure 17. As was the case with the velocity decay, the present measurements indicate a higher decay constant; they also seem to follow less accurately the $-\frac{1}{2}$-power law but would be better represented by a law with a larger negative exponent. Further, there is a very noticeable levelling-off of the temperature near the free surface where it assumes approximately constant values. This indicates the region of the flooded hydraulic jump where there is no further entrainment of ambient water but only re-entrainment of heated water. This behaviour and also the decay law becomes even clearer in figure 18 where the excess-temperature decay is plotted according to the scaling law of Chen & Rodi (1980) which again involves multiplication of $\Delta T_{\rm M}/\Delta T_0$ and the relative distance z/B with exponential functions of the Froude number F. It can be seen that the data follow quite well the decay laws proposed by Chen & Rodi (1980) for the individual regions when the upper jet zone with re-entrainment is excluded. In the intermediate region the decay exponent suggested is $-\frac{3}{4}$. This explains why in figure 17 the decay according to the $-\frac{1}{2}$ law in the non-buoyant region was not so well followed. In the upper portion of the jet the temperature remains virtually constant and this is the region where the submerged hydraulic jump involving a roller is present so that there is good mixing and re-entrainment of heated water. Outside this region, the temperature behaviour can again be seen to follow well-established laws. The fact that the data come to lie somewhat above the correlation of Chen & Rodi (1980) may again be because the ambient was not really stagnant in this case.

Figure 19 shows the development of the vertical turbulence intensity $\overline{w^2}^{\frac{1}{2}}/W_{\rm M}$ along the jet axis for various experimental situations. The distributions are compared with those measured in a free jet by Gutmark & Wygnanski (1976) and in a jet impinging on a wall measured by Gutmark *et al.* (1978). For the non-buoyant case there is fairly good agreement with Gutmark *et al.*'s (1978) distribution except very close to the surface. The approach towards the surface is at first very similar. Near the surface there is a strong rise in the relative w-intensity which is due to the fact that $W_{\rm M}$ drops sharply in this region (see figure 14) while the turbulence fluctuations are carried into the impingement region from upstream. Gutmark *et al.*'s (1978) measurements
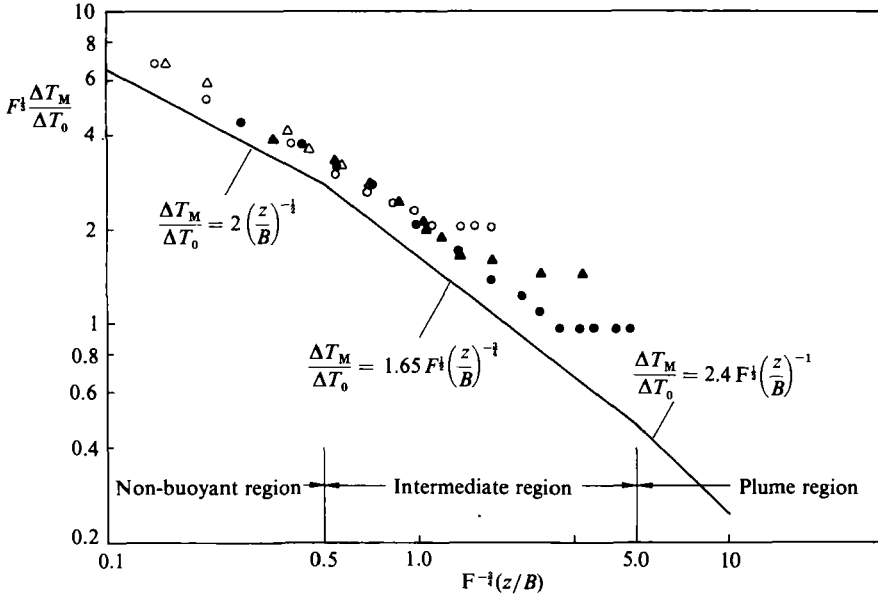
FIGURE 18. Centreline excess-temperature decay, symbols as in figure 17.
Solid line: correlation of Chen & Rodi (1980).

indicate, however, that very near the surface the relative intensity $\overline{w^2}^{\frac{1}{2}}/W_M$ decreases again which implies a very sharp drop in $\overline{w^2}$. Their hot-wire data are probably not very reliable in this region of high turbulence intensity (of the order of 50 %), but the drop can be explained by the damping of normal fluctuations by the wall (the fluctuations parallel to the surface are increased at the same time) and is sometimes also called the pressure-reflection effect. This effect was investigated in more detail by Thomas & Hancock (1977) for a situation near a moving wall with zero shear stress. Although a similar effect was observed to occur at the free surface of open-channel flow (see e.g. Komori et al. 1982), the relative intensity does not decrease very near the free surface in the present measurements. This is probably because, in contrast to the near-wall situation, the normal fluctuations $\overline{w^2}$ do not actually go to zero at the surface while the mean velocity W_M does.

5.2. Ambient channel region

A detailed mapping of the mean temperature in the whole flow field is provided in figure 20 for Froude numbers $F = 9.9$ and 21. Results for the unstable case with $F \to \infty$ are not shown as the temperature was uniform in the test section for the steady state. Figure 20 shows temperature profiles at various x-positions from the central plane $x/H = 0$ to the downstream plane $x/H = 2.46$. As temperature is probably the most reliable quantity to measure, the temperature profiles are an important indicator for the whole flow. Figure 20 shows that for both Froude-number cases there is a fairly thick upper heated layer with nearly uniform temperature. This layer is thicker in the higher-Froude-number case. The interface below this layer, characterized by the presence of a considerable temperature gradient, is indicated in figure 20 for the two Froude-number situations. This interface region covers that part of the depth where the temperature gradient $\partial T/\partial z > \epsilon(T_0 - T_a)/H$ with $\epsilon \approx 0.01$. The figure shows clearly that the interface region widens near the jet, which indicates that more mixing
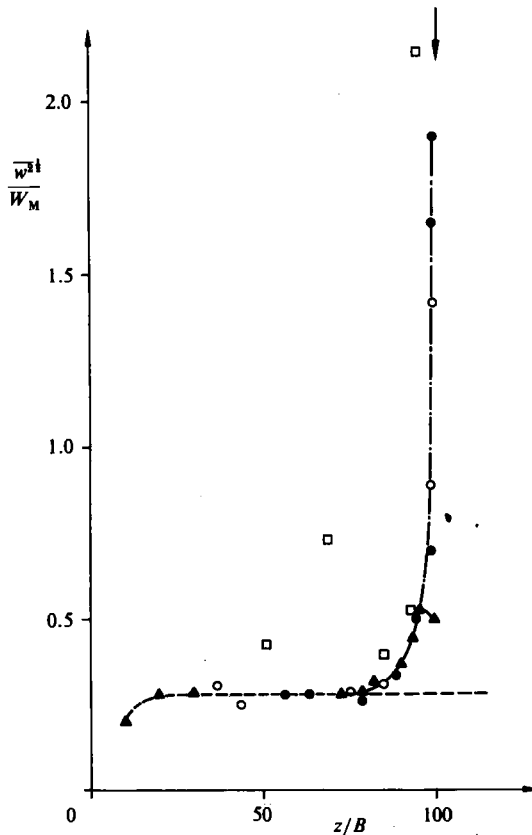
FIGURE 19. Turbulence intensity $\overline{w^2}$ on jet centreline. Present data: $\bigcirc$, $F = \infty$, $Re = 5197$, $H/B = 100.8$; $\bullet$, $F = \infty$, $Re = 2675$, $H/B = 100.8$; $\square$, $F = 9.9$, $Re = 2675$, $H/B = 100.8$; $\blacktriangle$, Gutmark *et al.* (1978): $F = \infty$, $Re = 30000$, $H/B = 100$, jet impinging on wall; ————, Gutmark & Wygnanski (1976), free jet.

is taking place there; this, in turn, points to the presence of a roller in this region. Below the interface is the ambient flow region in which cold water flows towards the jet to be entrained. In the case of $F = 21$, the interface nearly reaches the bottom, and probably intermittently does so as indicated by the dye picture in figure 9 (grey tone of fluid in lower layer). This shows that the flow is only marginally stable and that there appear to be moments when heated water reaches the bottom and is swept upstream and re-entrained into the jet. In the downstream region where the interface is relatively thin and hence the temperature gradient is sharp, mixing is strongly inhibited by the stable stratification. There is of course still molecular diffusion but this is fairly small, especially since the Prandtl number for water has the large value of 10. Assuming that there is a roller region with closed streamlines (see figure 22 for how these may look) the heated water and also the injected dye can get into this region only by diffusion and, as turbulent diffusion is inhibited by stable stratification and laminar diffusion is a rather slow process, it may take a very long time before dye penetrates into this region. This may be the reason for some apparent differences between the temperature profiles of figure 20 and the photographs shown in figures 8 and 9. There is however some correspondence between the two: for $F = 9.9$, the upper edge of the interface corresponds roughly to the edge of the dyed layer; for
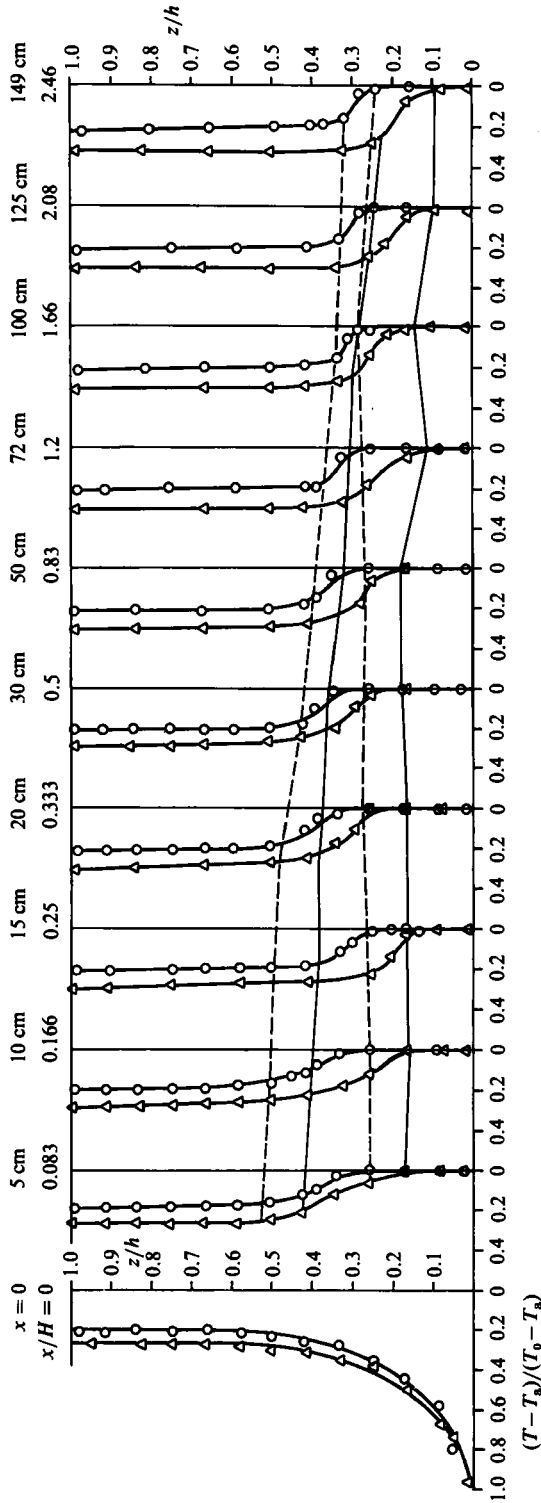
FIGURE 20. Mean temperature distribution: ○, $F = 9.9$, $Re = 2635$, $H/B = 100.8$; △, $F = 21$, $Re = 5197$, $H/B = 100.8$. Dotted and solid lines indicate regions with high temperature gradients for $F = 9.9$ and $F = 21$, respectively.

$F = 21$ it lies slightly below. Further, one should remember that low-concentration dye may not be visible in the pictures.

The observed form of the temperature profiles, in particular their uniformity over a large part of the upper layer, is in close agreement with previous measurements in situations involving an internal hydraulic jump (see e.g. JH; Baddour & Abbink 1983). It is fairly clear from the temperature profiles that no appreciable amount of ambient cold water is mixed into the upper layer, as otherwise its temperature would have to decrease in the downstream direction. There is of course mixing taking place within the roller region.

It may be interesting to compare the present temperature measurements with the results of the JH mixing analysis. In the mixed upper layer the measurements indicate a nearly constant relative excess temperature ΔT_u of 0.24 and 0.31 for the cases of $F = 9.9$ and $F = 21$ respectively. These values correspond to dilution ratios $S = \Delta T_0 / \Delta T_u$ of 4.16 and 2.6 respectively. According to the analysis of JH the dilution ratios at $H/B \approx 100$ should be 11 and 7 for the Froude numbers 9.9 and 21 respectively (as taken from their figure 13). As already shown, for the low-Froude-number case a stable situation prevails for which the JH mixing analysis gives the dilution ratio simply as the amount of fluid re-entrained divided by the jet discharge, the former being determined by a simple integral jet analysis. In the present experiment, the submerged jump reduces significantly the entrainment of ambient fluid so that the lower dilution ratio is not really surprising. For the higher-Froude-number case ($F = 21$), the JH analysis predicts an unstable situation with a lower dilution ratio than for the stable case discussed above. That the dilution ratio observed in the present measurements is even lower, even though the discharge appeared marginally stable, can be explained as follows. For unstable discharges, the JH mixing analysis is based on the assumption that a stratified counterflow forms past the primary recirculation zone and rests heavily on equations describing this counterflow. The analysis is therefore valid only for relatively long channels with the downstream control sufficiently far away from the jet for a counterflow as described by the equations to develop. This is certainly not the case in the present experiment. In fact a strong downstream control was imposed at about three water depths downstream of the jet, causing for this particular Froude-number a jump with high submergence and therefore large conjugate depth so that little overall entrainment of ambient fluid could occur. It can be concluded that, owing to the strong downstream control and the flooded hydraulic jumps caused by it, the mixing analysis of JH is not valid for either buoyant case investigated in this study.

Figure 21 shows measured velocity vectors at five sections for the unstable discharge with $F = \infty$ and $Re = 2637$. Owing to physical obstructions and the particular set-up of the LDA, measurements could unfortunately not be taken near the bottom. Hence there are no velocity vectors available in the lower region. Assuming that the flow is two-dimensional, some information on the flow in this region can be obtained from the law of continuity. Integration of the velocity profile at $x/H = 1.66$ over the positive U-velocity region yields a flow rate in the downstream direction of $7.8 V_0$, where $V_0 = \frac{1}{2} B W_0$ is the discharge flow rate of half the jet. The reverse-flow rate is therefore $6.8 V_0$ which requires an average reverse-flow velocity of $0.05 W_0$. The dotted velocity profile included in figure 21 would yield such a flow rate. Although the measurements do not show this explicitly, they indicate a large recirculation zone ending beyond the last measurement station, with the centre at about half-depth and at $x/H \approx 1.3$. This finding is in accordance with the dye picture of figure 7.
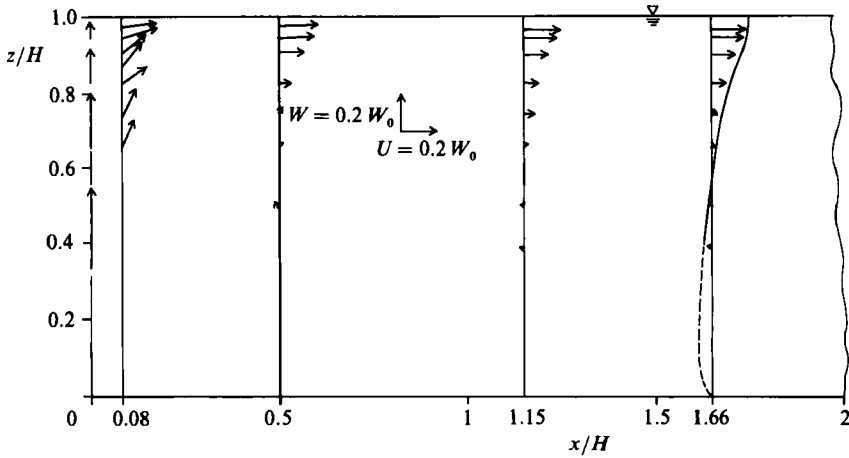
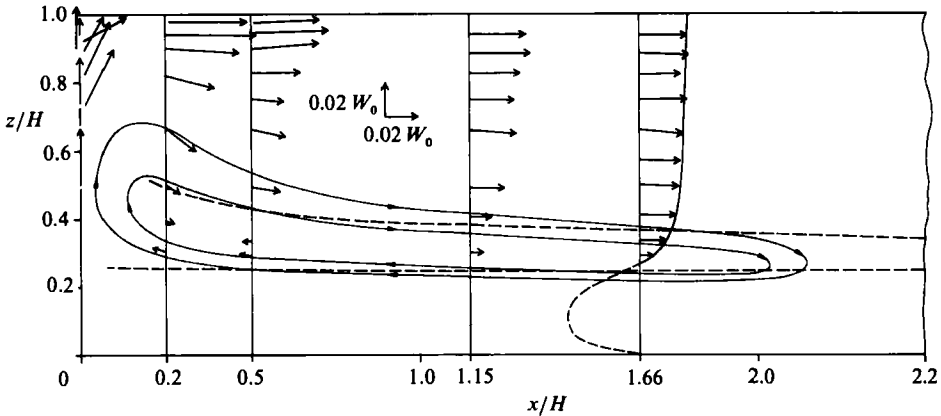FIGURE 21. Mean velocity vectors for the non-buoyant case: $F = \infty$, $Re = 2637$, $H/B = 100.8$.

FIGURE 22. Mean velocity vectors for the buoyant discharge at $F = 9.9$, $Re = 2635$,
$H/B = 100.8$.

The corresponding velocity vectors for the stable case with $F = 9.9$ are shown in figure 22. The dashed lines are included to indicate the edges of the interface as taken from figure 20. In the downstream region, where the local Froude number has fallen below 1, the velocity distribution can be seen to be fairly uniform over most of the upper layer. This behaviour is in agreement with previous observations that the velocity profile in buoyancy-dominated, subcritical layers is much more uniform than in non-buoyant shear layers (Wilkinson 1970; Rajaratnam & Subramanyan 1985). The integration of the velocity profile at $x/H = 1.66$ was carried out also in this case and yielded a downstream flow rate of $3.42V_0$. In this case therefore the reverse-flow rate has to be $2.42V_0$, requiring an average reverse-flow velocity of $0.045W_0$. A velocity profile consistent with this flow rate is indicated as a dashed line in figure 22. Since the change-over of the velocity profile occurs fairly close to the bottom, the reverse-flow has to be considerably larger than the downstream flow velocity. Unfortunately this was again in a region where no velocity measurements could be taken. A further check was however carried out. The heat flux in the upper layer where $U > 0$ and $\Delta T > 0$ was calculated at $x/H = 1.66$ from the relation $\int \Delta T U \, dz$ and was found to be 83% of the heat discharged by half the jet ($= \frac{1}{2}BW_0 \Delta T_0$). Taking into account some

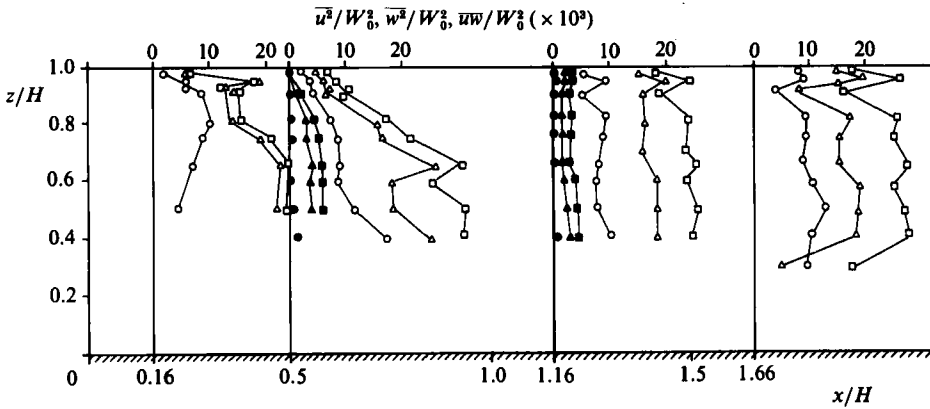$$\overline{u^2}/W_0^2,\ \overline{w^2}/W_0^2,\ \overline{uw}/W_0^2\ (\times 10^3)$$

FIGURE 23. Turbulent stresses for cases with $H/B = 100.8$, $Re = 2635$. $\overline{u^2}/W_0^2$: $\square$, $F = \infty$, $\blacksquare$, $F = 9.9$; $\overline{w^2}/W_0^2$: $\triangle$, $F = \infty$, $\blacktriangle$, $F = 9.9$; $\overline{uw}/W_0^2$: $\bigcirc$, $F = \infty$, $\bullet$, $F = 9.9$.

heat loss at the surface and at the sidewalls of a test channel, this appears to be a reasonable value, providing confidence in the level of the measured temperature and velocity profiles. A roller representing an internal hydraulic jump is not immediately obvious from the velocity-vector plot, partly owing to the incomplete picture given. However, such a roller can be imagined as sketched in figure 22 by two closed streamlines. The picture is certainly somewhat speculative but not inconsistent with the measurements. It is clear that the roller must contain regions with both positive and negative U-velocity and that it is a region where fairly strong mixing takes place so that the interface area with density gradients is believed to make up a large part of the roller region.

Figure 23 shows the distribution of the turbulent normal stresses $\overline{u^2}$ and $\overline{w^2}$ and of the shear stress $\overline{uw}$ at several x/H-locations for the non-buoyant, unstable case with $F = \infty$ and $Re = 2365$ and for the stable case with $F = 9.9$. The data are somewhat scattered, but they demonstrate clearly that the turbulent fluctuations are much smaller in the stable case. This is due to the fact that the turbulence-producing velocity gradient $\partial U/\partial z$ is quite small over most of the flow and, where it is large, strong stable density stratification prevails which damps the turbulence. In the unstable case, there are significant velocity gradients over most of the depth and there is no stable stratification. The shear-stress correlation $R_{uw} = \overline{uw}/\overline{u^2}^{\frac{1}{2}}, \overline{w^2}^{\frac{1}{2}}$, which is often taken as a measure of the turbulence structure, is also strongly affected. While it takes values of 0.4–0.5 typical of fully turbulent non-buoyant flows in the unstable case, R_{uw} is only of the order of 0.1–0.2 in the stable case with stratification.

6. Conclusions

The present flow-visualization, mean-velocity and temperature as well as turbulence measurements in the flow field generated by a buoyant line source discharging into shallow water complement the previous study of JH and allow a number of interesting conclusions. For the limiting case of non-buoyant discharges, the previous finding was confirmed that an unstable flow situation develops with a primary recirculation cell of about $2.5H$ length which drives a secondary cell further away from the discharge. In the buoyant situations, the flow development was found to depend strongly on the downstream control. A clearly identifiable roller representing

an internal hydraulic jump could be obtained in the relatively short test section only when a strong downstream control was imposed by a weir, the relative depth was below a certain value ($H/B < 116$) and the densimetric Froude number small ($F < 30$). A strong control placed fairly close to the jet caused the internal hydraulic jump to be flooded in both of the Froude-number cases investigated in greater detail. In both cases fairly thick upper layers with nearly uniform temperature developed which reached the jet, so that the temperature in the upper part of the jet was also constant at the level of the layers. This indicates re-entrainment of heated water into the jet and shows clearly the interaction of the jet with the roller of the hydraulic jump. In fact, in this interaction region the flow does not really have a clear jet behaviour. Below the constant-temperature layer, an interface with a temperature gradient develops which thickens towards the jet, indicating mixing in the roller region. Below this interface layer there is a counterflow of ambient, cold fluid which is entrained into the jet. For the higher-Froude-number case, the depth of this ambient fluid layer is rather small so that the heated layer nearly reaches the bottom, and seems to do so intermittently. This indicates that, in the higher-Froude-number case, the flow is at the verge of instability, i.e. it tends to develop a recirculation in the near-jet region.

There is considerable agreement with the analysis of JH, which was verified by their experiments, concerning the stability of the flow and the hydraulic-jump behaviour. The influence of the relative depth H/B and of the densimetric Froude number F on the flow pattern and in particular on the conjugate depth of the upper layer follows the trends established by the analysis of JH. The same is true for the stability of the flow. On the other hand, the dilution of the discharged heated water cannot be described by the mixing analysis of JH. The different dilution behaviour is due to the relatively short test channel ($\approx 3.3H$ in most experiments as compared with $10H$ in the case of JH) and the imposed strong downstream control which, in contrast to the analysis and experiments of JH, caused the internal hydraulic jump to be flooded and prevented the development of a significant stratified counterflow region. The flooded jumps reduced significantly the entrainment of ambient fluid into the jet and therefore led to a considerably lower dilution than predicted by the analysis and measured in the experiments of JH. These authors' dilution analysis is therefore not valid for the present cases. The differences observed between the present and the JH experiments will certainly form an interesting and severe test for any mathematical model for simulating buoyant-jet-in-shallow-water configurations.

Finally, the measured behaviour of both the buoyant and non-buoyant vertical jets in the regions not influenced by the free surface or by the flooded hydraulic jump corresponds closely to established free-jet laws. The velocity and excess temperature levels are slightly higher than indicated by the correlation of Chen & Rodi (1980). This difference is probably caused by the fact that the ambient is not really stagnant but moving because of the confinement.

Appendix. Determination of the LDA bursting frequency from the frequency spectrum

The digitized signals of the LDA burst, which included at least 20 cycles, were evaluated to determine the frequency spectrum and also the bursting frequency. To this end, Fourier transforms of two real-value records were computed simultaneously by inserting one record $x(n)$ as the real part and one record $y(n)$ as the imaginary part of a complex record $z(n)$ (see Bendat & Piersol 1971).

Let

$$z(n) = x(n) + \mathrm{j}y(n) \quad (\cdot = 0, 1, ..., N-1).$$ (A 1)

The Fourier transform of $z(n)$ is

$$Z(k) = \sum_{n=0}^{N-1} [x(n) + \mathrm{j}y(n)] \exp\left[-\mathrm{j}\frac{2kn}{N}\right] \quad (k = 0, 1, 2, ..., N-1)$$

and the two real-valued records $x(n)$ and $y(n)$ have Fourier Transforms $X(k)$ and $Y(k)$ given by

$$X(k) = \frac{Z(k) + Z^*(N-k)}{2},$$

$$Y(k) = \frac{Z(k) - Z^*(N-k)}{2\mathrm{j}},$$

where Z^* is the conjugate complex number of Z. This has been computed using a FORTRAN code for a decimation-in-time, in-place FFT after Cooley, Lewis & Welsh (1969). Thus a complex record/array of 2^{11} values was fast-Fourier transformed (FFT) twice thus allowing a direct determination of the Doppler frequency at both channels. It should be pointed out that without the use of (A 1), 4 FFT's would be required to obtain the power spectra for both channels. In order to increase further the accuracy in determining the bursting frequency, a second-order interpolation scheme was used in which a curve through three points around a maximum value in the power spectrum was fitted.

REFERENCES

BADDOUR, R. E. & ABBINK, H. 1983 Turbulent underflow in a short channel of limited depth. *J. Hydraul. Engng ASCE* **109**, 722–740.

BADDOUR, R. E. & CHU, V. H. 1975 Buoyant surface discharge on a step and on a sloping bottom. *Tech. Rep. No.* 75-2 (FML). Department of Civil Eng. and Applied Mech., McGill University, Montreal, Canada.

BENDAT, J. J. & PIERSOL, A. G. 1971 *Random Data: Analysis and Measurement Procedures*. Wiley.

CHEN, C. J. & RODI, W. 1980 *Vertical Turbulent Buoyant Jets – A Review of Experimental Data*. HMT Series, vol. 4, Pergamon.

COOLEY, J. W., LEWIS, P. A. W. & WELCH, P. D. 1969 The finite Fourier transform. *IEE Trans. Audio- and Electroacoustics*, AV-17, 77–85.

DURST, F., MELLING, A. & WHITELAW, J. H. 1981 *Principles and Practice of Laser Doppler Anemometry*, 2nd edn. Academic.

DURST, F. & TROPEA, C. 1977 Processing of laser-Doppler signals by means of a transient recorder and a digital computer. *Rep.* SFB 80/E/118. University of Karlsruhe.

GUTMARK, E., WOLFSHTEIN, M. & WYGNANSKI, I. 1976 The plane turbulent impinging jet. *TAE Rep. No.* 226. Technion, Haifa, Israel.

GUTMARK, E., WOLFSHTEIN, M. & WYGNANSKI, I. 1978 The plane turbulent impinging jet. *J. Fluid Mech.* **88**, 737–756.

GUTMARK, E. & WYGNANSKI, I. 1976 The two-dimensional turbulent jet. *J. Fluid Mech.* **73**, 465–495.

JIRKA, G. H. 1982*a* Multiport diffusors for heat disposal: a summary. *J. Hydraul. Div. ASCE* **108**, 1425–1468.

JIRKA, G. H. 1982*b* Turbulent buoyant jets in shallow fluid layers. In *Turbulent Buoyant Jets and Plumes* (ed. W. Rodi), HMT Series, vol. 6. Pergamon.

JIRKA, G. H. & HARLEMAN, D. R. F. 1979 Stability and mixing of a vertical plane buoyant jet in confined depths. *J. Fluid Mech.* **94**, 275–304.

KOMORI, S., UEDA, H., OGINO, F. & MITZUSHINA, T. 1982 Turbulence structure and transport mechanism at the free surface in an open channel flow. *Intl J. Heat Mass Transfer* **25**, 513–521.

LEE, J. H. W. & JIRKA, G. H. 1981 Vertical round buoyant jet in shallow water. *J. Hydraul. Div. ASCE* **107**, 1651–1675.

MEHROTA, S. C. 1976 Length of hydraulic jump. *J. Hydraul. Div. ASCE* **102**, 1027–1033.

RAJARATNAM, N. & SUBRAMANYAN, S. 1985 Plane turbulent buoyant surface jets and jumps. *J. Hydraul. Res.* **23**, 131–146.

RAMAPRIAN, B. R. & CHANDRASEKHARA, L. S. 1983 Study of vertical plane turbulent jets and plumes. *IIHR Rep. No.* 257. The University of Iowa.

TENNEKES, A. & LUMLEY, J. L. 1972 *A First Course in Turbulence*. MIT Press.

THOMAS, N. H. & HANCOCK, P. E. 1977 Grid turbulence near a moving wall. *J. Fluid Mech.* **82**, 481–490.

WILKINSON, D. L. 1970 Studies in density-stratified flows. *Rep. No.* 118. School of Civil Engineering, University of New South Wales, Australia.

WILKINSON, D. L. & WOOD, I. R. 1971 A rapidly varied flow phenomenon in a two-layer flow. *J. Fluid Mech.* **47**, 241–256.